MILLIMETER-WAVE RECEIVERS FOR WIRELESS COMMUNICATIONS

by

Brock Morgan Overmiller

A thesis submitted to the Faculty of the University of Delaware in partial fulfillment of the requirements for the degree of Master of Science in Electrical and Computer Engineering

Spring 2016

MILLIMETER-WAVE RECEIVERS FOR WIRELESS COMMUNICATIONS

by

Brock Morgan Overmiller

Approved: _____
Dennis W. Prather, Ph.D.
Professor in charge of thesis on behalf of the Advisory Committee

Approved: _____
Christopher A. Schuetz, Ph.D.
Co-Professor in charge of thesis on behalf of the Advisory Committee

Approved: _____
Kenneth E. Barner, Ph.D.
Chair of the Department of Electrical and Computer Engineering

Approved: _____
Babatunde A. Ogunnaike, Ph.D.
Dean of the College of Engineering

Approved: _____
Ann L. Ardis, Ph.D.
Senior Vice Provost for Graduate and Professional Education

ACKNOWLEDGMENTS

With unbound appreciation, I would like to take a moment to extend my gratitude to those who have helped guide and support me to the end. I would like to thank my advisors, Dr. Prather and Dr. Schuetz, for providing me with this amazing opportunity and their unwavering advisement to see me succeed and grow in the field of RF Photonics research.

I would also like to thank all of the members within Dr. Prather's research community. Working alongside the many brilliant fellow graduate students and even more brilliant post-docs has impacted my life and research in such a positive way. This work would have been a steeper uphill climb if not for your willingness to help and answer questions when needed. I would also like to thank the employees at Phase Sensitive Innovations (PSI) for their support and knowledge of passive millimeter-wave imaging. If not for PSI, none of this research and work would have been possible. The friendships made will last a lifetime.

To my family and friends, thank you for your support in helping pave the road to this part of my life's journey. I really appreciate the countless hours you have set aside throughout the years to teach me new life lessons that have steered me be the person I am today. Especially to my parents, thank you for always believing in me and comforting me in difficult situations. I want to thank my siblings, Dusty and Dena, for being my role models. Nothing is more exciting than striving to be the smartest sibling. Lastly, thank you Diana for the support you provided every step of the way.

TABLE OF CONTENTS

LIST OF TABLES

LIST OF FIGURES

ABSTRACT

The modern communications environment is becoming an increasingly crowded place, resulting in rapidly increasing demands on current technology. Military and civilian operations require the ability to locate and decode all communication signals in the environment. However, developments in RADAR (RAdio Detection And Ranging) and communications technology are making it harder to effectively identify and maintain bandwidth usage for everyone. Millimeter waves - waves measured between one millimeter to one centimeter in wavelength - have only recently been explored as a new technology to replace the augment receiver architectures. These small wavelengths introduce many engineering challenges, such as: large atmospheric losses, poor sensitivity, and expensive electronic equipment. With growing developments in Microwave Photonics, low-noise RF amplifiers and high-speed modulators have demonstrated the ability to design RF communication links in the millimeter wave regime to counter such problems. However, despite these developments, toward a cost-effective, spatial division multiplexing (SDM) receiver concept has not proved capable of being implemented as part of the next generation 5G wireless network infrastructure.

To this end, we present a novel receiver architecture utilizing an optically addressed phased-array millimeter wave receiver based on optical-upconversion and signal recovery. This receiver is capable of geolocation and spatial multiplexing of multiple Tunable Optically Paired Source (TOPS) communication signals in its scene. Operating at 35 GHz, the receiver up-converts the received RF onto an optical

sideband, which, to our advantage, contains all of the frequency, amplitude, and phase information of the received signals. Subsequent optical processing allows routing of the sideband to a free space detector port. Photomixing a coherent optical local oscillator (LO) with the optical sideband performs heterodyne down-conversion to an Intermediate Frequency (IF) where we are able to spatially resolve each signal individually to recover complex modulated formats transmitted by our TOPS generators.

In this thesis, we describe the unique advantages of our receiver concept to allow for frequency re-use as well as cell sectoring methods to increase the overall data capacity bandwidth. Primarily, the use of a distrusted aperture array enables high resolution imaging, limited only by the diffraction efficiency set at the antenna array. Thus, angle-of-arrival (AoA) capabilities help deduce the position of each signal and the data it contains. Unlike IR or visible wavelengths, millimeter waves have the unique ability to penetrate dust, smoke, cloud coverage, and thin fabrics such as clothing. As such, millimeter wave receivers have the capability of achieving high signal-to-noise ratios (SNR) in obscured environments compared to their counterparts.

This optically addressed communication receiver offers vast advantages over current communication receiver architectures in place today. This approach has the potential to operate as the next generation communication receiver for 5G wireless. In addition, this receiver concept appeals to many security and defense applications requiring secure communications and unwanted signal avoidance.

Chapter 1

INTRODUCTION

1.1 Key Metrics for Wireless Communications

Every day, thousands of people reach into their pocket and grab their phone to text or call their loved ones, play virtual games to pass time, or check for updates to their emails and social networks. The backbone to such unbelievable capability dates back to the late 1900's when Alexander Graham Bell and his associate, Charles Sumner Tainter, invented the photophone [1]. They demonstrated the first ever wireless audio conversation. Their work has led to advancements in wireless technologies, based between 800 MHz to 5 GHz, i.e., LTE, Wi-Fi, Bluetooth, and AM/FM radio. The modern communications era is flourishing with more and more people buying cellular phones, wireless internet tablets, and video gaming systems. However, this thriving era is slowly starting to reach its maximum capability. With the growing advancements in user technology, the communication environment will reach its bandwidth bottleneck in the near future. In addition, wireless communication receivers are having a harder time multiplexing each incoming signal to relay the encoded data.

Given the frequency band usage, increasing the allowable bandwidth around 2.4 GHz is nearly impossible, and implementing improved receivers is very costly considering the lack of available bandwidth remaining. Fortunately, there exists a frequency band that has many benefits for communications technology, but has only recently been explored. The frequency band between 30 - 300 GHz has widely been

disregarded due to lack of electronics and cost effective detectors. This band is considered the millimeter-wave regime, as the wavelengths in this band are measured between 1 mm to 10 mm in length. Millimeter waves offer an abundant amount of advantages and capabilities compared to the current communication band. As a start, millimeter-waves have a unique property in that their radiation waves can penetrate obscurants such as dust, clouds, and fog leading to poor weather avoidance. Higher frequencies offer improved angular resolution while reducing the aperture size necessary at the receiver. Meaning, the current aperture receiver will produce more highly resolute images in the millimeter-wave range, giving way to virtually unlimited bandwidth for communication networks.

1.1.1 Link Budget Effects on Data Capacity and Throughput

Developing a new communication network first requires the consideration of key metrics of wireless communication. First and foremost is the trade-off between the link budget of the network and the data capacity that can be received and decoded. Figure 1-1 illustrates a typical communication link budget accounting for the gains and losses in the entire system.

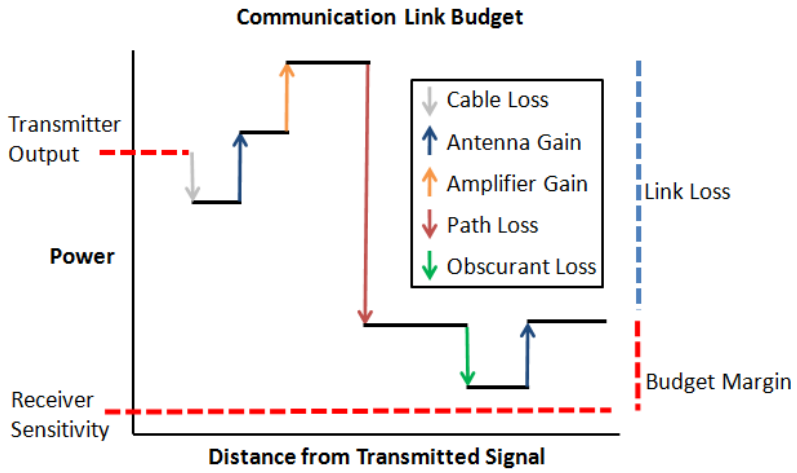

Figure 1-1: Communication Link Budget

[2]

In terms of a wireless communication link, there are three extremely essential parts: transmitter, receiver, and the transmission medium. A transmitter first defines the overall performance of the link budget. Typically, a transmitter consists of an amplifier and an antenna. The amplifier adds a precise amount of power to the transmitted signal and an antenna provides further gain. To generate a communication signal, an RF or microwave signal at a designated frequency is modulated to contain the data information. After cable loss and gains from the amplifier and antenna, the output signal is at its maximum signal-to-noise ratio (SNR). However, depending on the distance, d, between the transmitter and receiver, and the frequency, f, of transmission, there will be substantial RF path loss given by Friis Equation [3],

$$L_{FS} = \left(\frac{4\pi df}{c} \right)^2 . \tag{1-1}$$

In addition, any obscurants or obstacles will act as attenuators to the signal strength. At the receiver, the communication signal is received in the noise and amplified with sufficient enough SNR to demodulate and route the received signal to a central processing location. Given a precise modulation technique, the signal-to-noise ratio is the most essential aspect for link budget analysis. In order to determine the SNR of the link: the data rate, R, overall system bandwidth, B_T, and the bit energy per noise-density, ($\frac{E_b}{N_0}$), must all be known [4]

$$SNR = \left(\frac{E_b}{N_0}\right) * \left(\frac{R}{B_T}\right). \tag{1-2}$$

With regards to signal quality, the most important figure of merit is the Bit Error Rate (BER). BER signifies how many bit errors are decoded in the data stream. Due to noise contributors or signal distortion, the BER can be distorted. Generally, the best links have extremely low bit error rates, on the order of 10^{-14} and better [5][6]

$$BER = \frac{1}{2} erfc\left(\sqrt{\frac{E_b}{N_0}}\right). \tag{1-3}$$

However, wireless links are limited by the receiver sensitivity, or the necessary signal strength at the input of the receiver to be above the noise floor. A higher RF noise floor will require a greater transmission signal to maintain good SNR through the system to analyze the transmitted modulation format. Implementing a phased-array receiver rather than a single isotropic antenna will further increase the overall gain of the system by the use of space division multiplexing within the central processing location.

1.1.2 Space Division Multiplexing (SDM)

Phased-array receivers are extremely advantageous for wireless networks. By applying phase shifts to each of the receiving antennas, they will constructively and destructively interfere with each other to steer the receiver to desired locations [7]. This gives way to angle-of-arrival detection. This means each emitting transmitter will arrive at the receiver at a unique angle of incidence. In the back-end processor, these spatially diverse signals will map to specific locations on the image plane. This ability renders the receiver capable of spatially multiplexing every transmitter in the scene without the worry of interference from other transmitters. Additionally, phased-arrays prove advantageous with their high gain and side lobe suppression. Furthermore, designing a distributed aperture array with many channels will suppress the side lobes even more while increasing the gain proportional to the number of antennas in the system. As such, an SDM receiver is capable of the channelization of all received signals onto their own detectors. Figure 1-2 illustrates the Spatial Division Multiplexing capabilities of our receiver. Here, signals emitting from transmitter "1" are all mapped to the bottom detector, transmitter "2" is mapped to the upper detector, and on-axis transmitter "3" is mapped to the middle detector. This approach can be scaled to all other signal in the scene of the receiver. This achieves spatial channelization from each sector.

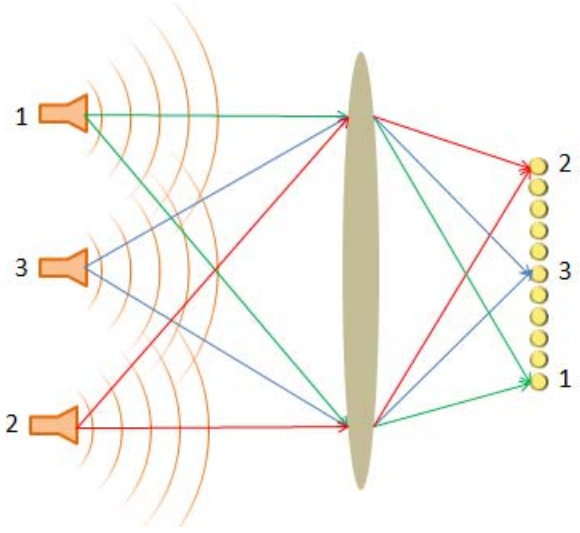

Figure 1-2: Spatial mapping of signals after arriving at a receiver from different angles onto separate locations of the receiver plane detector

1.2 Beamspace MIMO Techniques for Improved Com Receivers

With the vast expansion of wireless device technology, more consumers are flooding communication towers, proving the need for improved network infrastructures. Phased-array millimeter wave imaging systems are surfacing as the front runners for replacement. Millimeter wave systems offer wider bandwidths and easier signal sectoring methods through multiple-input multiple output (MIMO) techniques. SDM receivers require a MIMO antenna design. Wirelessly, MIMO techniques are accomplished in the beamspace. Beamspace MIMO proliferates data capacity by exploiting numerous incoming signals, including multipath transmission to individual output detectors [8]. Communication receivers implementing beamspace MIMO techniques notice significantly more spectral efficiency by spatial multiplexing of simultaneous data streams [9]. Given an antenna array aperture, the small wavelengths at millimeter wave frequencies offer higher angular resolution. In combination with MIMO techniques, millimeter wave receivers offer high data rate

throughputs for wireless communication networks, including frequency reuse for unlimited spectral bandwidth.

1.2.1 Cell-Splitting and Sectoring Methods for Increased Channel Capacity

The ability of a receiver network to improve its spectral bandwidth in each detector cell is restricted due to poor signal-to-noise. Interference contributions play a large role in limiting the SNR, or specifically the co-channel interference (CCI) and adjacent channel interference (ACI). Co-channel interference is the transmission of two or more communication signals emitting at the same frequency, creating crosstalk in the receiver. Adjacent channel interference is a result of unwanted signal emission from an adjacent frequency channel due to spectral impurity or poor frequency bandwidth control. To minimize interference, frequency reuse patterns must be staggered to direct the energy onto a different detector as shown in Figure 1-3. Here, a set of 7 different frequencies can be detected within a cluster of adjacent cells. Frequencies are then reused in a new cluster of frequencies improving the total bandwidth of the system to the original bandwidth times the cluster size occupied within a single cell. Frequency reuse distance can be determined by the cluster size, N, and the radius of the cell, R,

$$D_R = \sqrt{3N} * R. \tag{1-4}$$

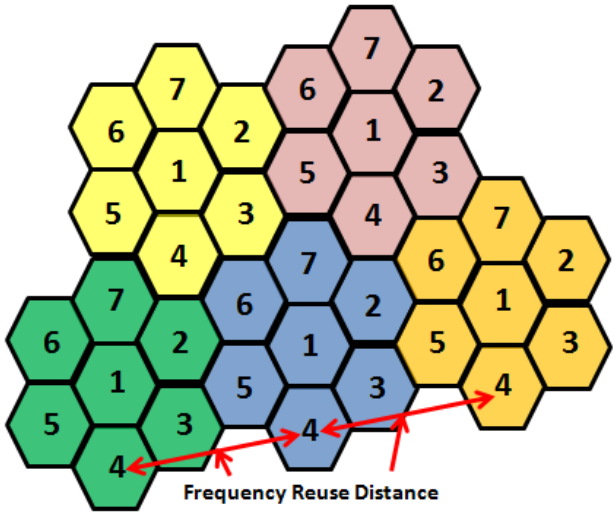

Figure 1-3: Frequency Reuse through cell staggering [10]

Inside the clusters, another process can take place to further improve frequency reuse, ultimately increasing the system bandwidth. Cell splitting, the process of subdividing congested cells in the cluster into small clusters [11], reduces the original cell size. Thus more cells must be employed, as displayed in Figure 1-4. Consequentially, the new cells must reduce their emission power so not to interfere with the transmitted signals within the original cells. However, this places added burden on the network infrastructure and increases the complexity of the back-end processor. In contrast to Figure 1-4, not all cells are split causing simultaneous allocation of split and un-split cells. Each cell splitting method would require its own BS antenna with ultra-fine angular resolution or separation reduction between the BS and the ground. Ultimately, designing complex cell splitting methods has the potential to significantly increase data capacity of the wireless network.

Figure 1-4: Typical cell cluster (left) and cell splitting process (right) [12]

Another method to improve data capacity is through cell sectoring. At the base station (BS), rather than using an omni-directional antenna, cell sectoring involves replacing the existing topology with multiple anisotropic antennas [13]. In doing so, factors such as CCI and ACI are reduced while adding gain to the received signals from the directive antennas improving the SNR and dynamic range.

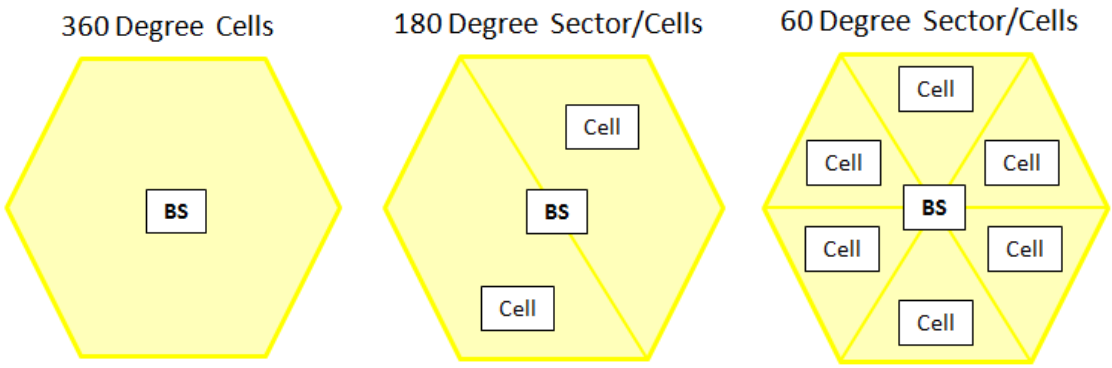

Figure 1-5: Cell Sectorization Method using multiple directional antennas [14]

Figure 1-5 displays the ability of cell sectoring to increase the amount of cells around a single base station. As more antennas are implemented into the BS, wider bandwidths can be achieved, however, scalability and costs are the current limiters.

1.3 Potential Applications for the Proposed Receiver

One of the prime principles of designing a new receiver is the potential applications for full scale integration. To our knowledge, we have realized the first ever communication receiver capable of beam forming received signals from a phased array based on optical sampling and image reconstruction. We have explored concepts for integrating our receiver into military and civilian operations. Military operations require the ability to locate and identify signals of interest while isolating unwanted signals at the detector. However, increasing developments in RADAR and communications technology are making it hard to effectively identify these emissions. In order to differentiate signals in the scene, a phased-array system must be used to achieve AoA detection. Figure 1-6 illustrates our low cost, size, weight and power (CSWAP), broadband phased-array RF receiver capable of spectral and temporal signal identification when coupled with a high-speed photodetector.

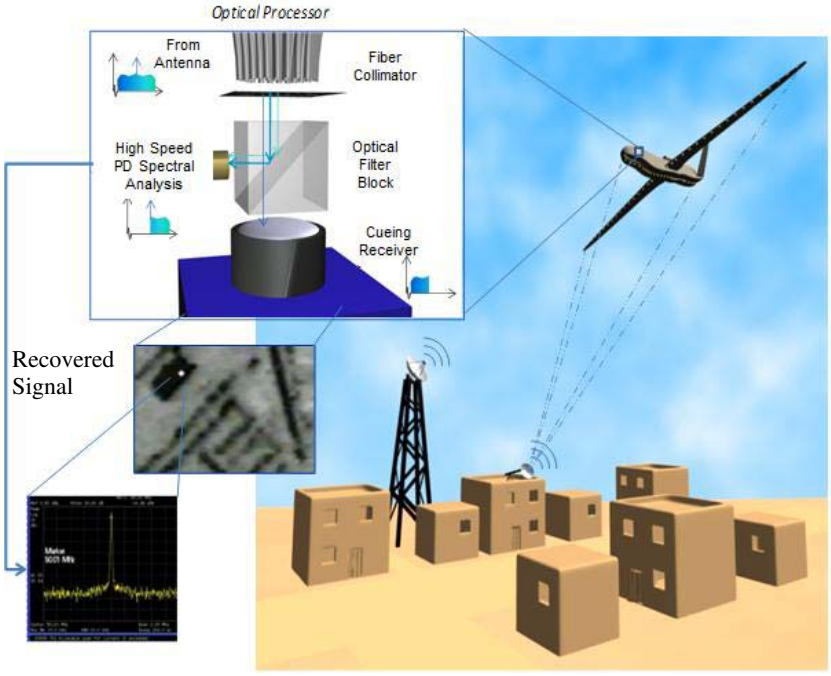

Figure 1-6: Conceptual realization of millimeter-wave receiver with capabilities for spectral and temporal signal identification

Additionally, secure communications between bases and troops provides further safety to those in dangerous areas. If communication signals were to be received and detected by unwanted listeners, plans may be compromised. This receiver is capable of safe messaging through IF detection and recovery.

Civilian operations are of utmost importance. For instance, increasing the consumer usage of wireless devices, the current wireless network architecture will not be able to maintain bandwidth, or data coverage, as seen in Figure 1-7. By implementing optically addressed phased array communication receivers as demonstrated in this thesis, we can achieve extremely wide bandwidths while spatially multiplexing clusters of cells for grater spectral coverage. A wireless network to support unlimited systems, services, and communications devices is now possible.

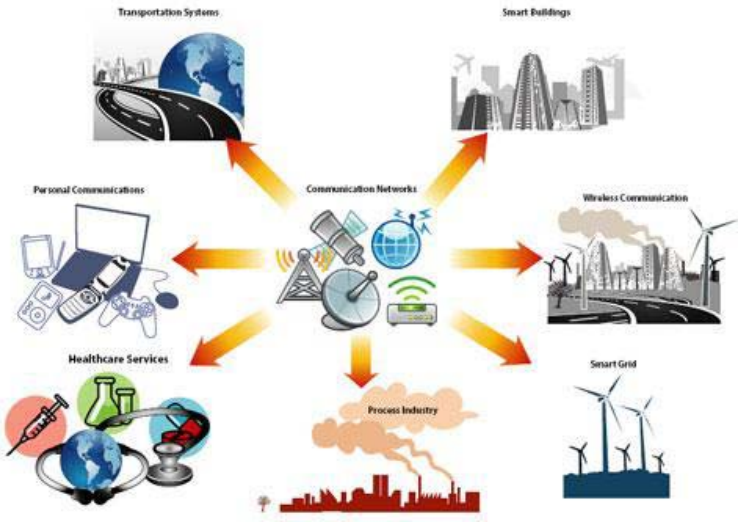

Figure 1-7: Current wireless communication network [15]

Bandwidth is surely the holdup for 5G wireless networks, but not the only issue concerning the current architecture. RF components and cables for signal routing at

higher frequencies are becoming very expensive. Cables specifically are very bulky and heavy in nature while introducing magnitudes of loss as the length of the cables increase. Instead, optical fiber can be utilized to afford low-loss, dispersion-less routing for long haul data transmissions. Moreover, optical fiber can be easily integrated into wireless network architectures due to their incredible flexibility and robustness. This thesis details the underlying associated optical and photonic components enabling millimeter wave receiver systems for communication networks.

1.4 Novel Contributions and Thesis Outline

Introduced in this thesis is the development and demonstration of a passive millimeter wave receiver based on optical techniques for next generation 5G wireless networks. This receiver operates at 35 GHz, currently offering 3 to 5 GHz allowed bandwidth compared to the current network architecture of 2 GHz, with methods detailed above to offer significantly greater capacities. This thesis addresses the primary concerns associated with expanding issues surrounding data haul capabilities and the enhancements made to the receiver to combat the growing issues.

Chapter 2 describes the RF receiver concept and the requirements necessary for phased array capabilities. Enabling technologies that define the operation of the communication receiver are also discussed. Taking a passive scene imager and implementing active scene detection is examined as well.

In Chapter 3, the design and characterization of a tunable optically paired source (TOPS) generator is described in great detail. This TOPS generator allows us to generate any microwave or millimeter wave frequency between 1-110 GHz, with the possibility of generating up and exceeding 200 GHz. The required components and the high-speed photodiodes will be discussed as well.

Chapter 4 will discuss the initial results of the receiver's capability to detect active sources in the scene. The calibrations made to the detector port to offer the ability to spatially multiplex multiple sources are explained. Lastly, power characterizations through beam steering are illustrated to match the calculated angular resolution and diffraction efficiency of the system from simulation.

After proving the receiver had the capability to isolate signals spatially at 35 GHz, we needed to develop a system to allow for low frequency detection. Chapter 5 explains the build and test of an optical local oscillator (LO) used in tandem with the imaging receiver to convert the received RF to an intermediate frequency (IF) for spectral analysis. As such, a high-power LO can be used with a high-power, low-speed photodiode to provide higher SNR and tunability for bandwidth optimizations. The components and schematic of operation are also included.

In Chapter 6, we begin to discuss the measurements and test setups created to arrive at wireless communication receiving and decoding. Experiments utilizing AM and FM modulation schemes are described. Each scheme helped pave the path to transmitting and receiving complex modulation formats. Furthermore, Chapter 6 illustrates the receiver's ability to spatially multiplex co-channel interference and decode solely the signal of interest rather than all other signals in the scene. Our phased array results are compared to the results found using a single conventional antenna.

Finally, Chapter 7 summarizes the thesis and the potential of our receiver concept to be implemented into the next generation communication network. Additionally, future improvement and optimizations to the millimeter-wave imager are described and the benefits associated with each one.

Chapter 2

RF RECEIVER CONCEPT

2.1 Design of a Passive mm-Wave Imaging Receiver

To offer optimal capability to construct a communication receiver, we built a proof of concept imager, relying on passive reception. In this Chapter, we detail the underlying RF photonic techniques used in converting RF energy to optical energy for routing and processing as well as the ability to multiply a singular link into a multi-channel millimeter-wave receiver. This research effort leverages an existing 35 GHz system approach utilizing novel techniques to upconvert the RF scene to the optical domain for passive imagery [16] and optimizing for active imagery as well. Operating at wavelengths between 1 to 10 millimeters, original investigations concerned the ability to combat military concerns such as brownout mitigation [17].

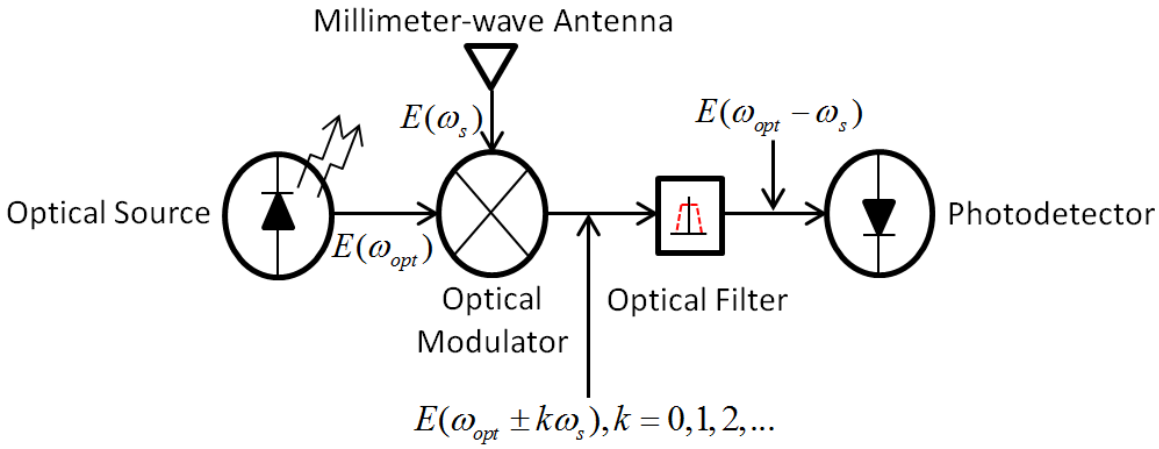

Figure 2-1: Conceptual RF Photonic Link of Communication Receiver

Figure 2-1 demonstrates a conceptual approach to receive millimeter-wave frequencies, filter the scene information, and route the optical field to a photodetector for electrical processing. We apply the optical source to seed multiple electro-optic modulators, each with a separate RF front-end consisting of a millimeter-wave antenna and a low noise amplifier (LNA) to amplify the weakly detected scene. The output of the modulators can then be applied to a micrometer scale replication of the antenna array, called a fiber array [18]. A custom fiber array design can translate the RF scene to an optical scene in free space as shown in Figure 2-2 (top).

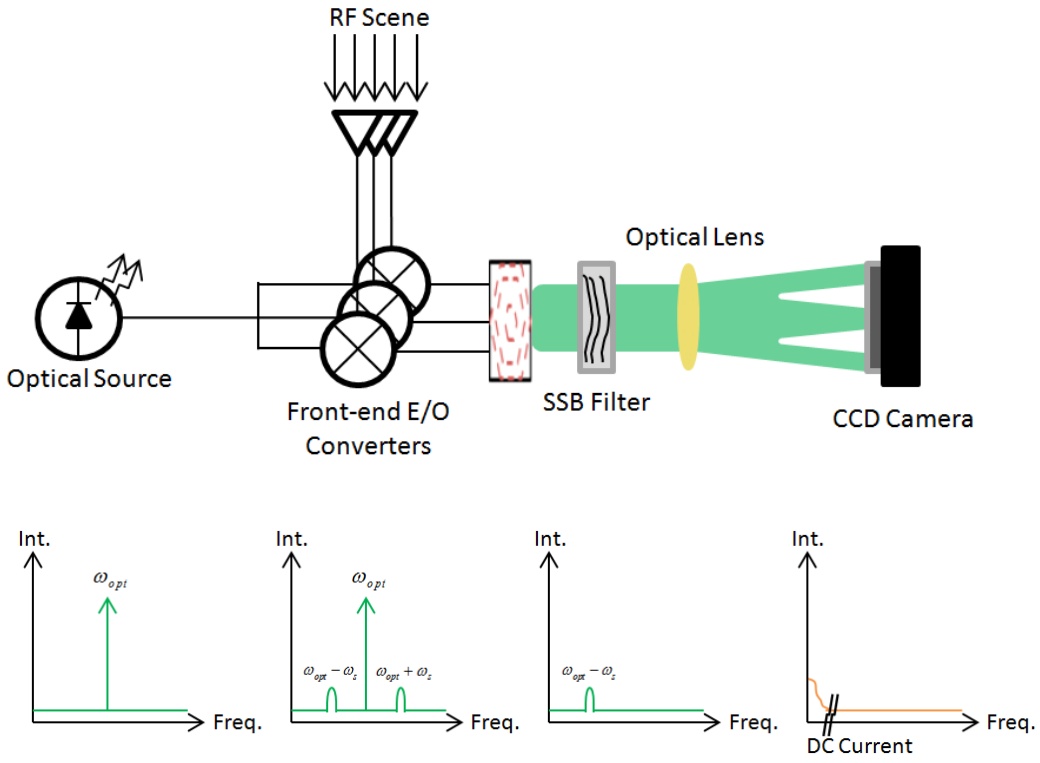

Figure 2-2: Schematic of RF to optical free space for spatial imaging (top) and optical spectrum through E/O conversion and photodetection

Once in optical free space, optical band-stop filters are used to pass only one sideband, $\omega_{opt} - \omega_s$. Using optical lenses, we are able to diverge all of the beams to overlap with each other at an image plane. Placing a SWIR camera at the image plane, image reconstruction of the scene is possible. Following Figure 2-2 (bottom), the optical source outputs an optical wavelength and upconverts the received RF to an upper and lower sideband; the carrier and the upper sideband are filtered out, and the passband lower sideband is sent to the charge-coupled device (CCD) to convert to electrical current to generate imagery based on current density on the detector pixels.

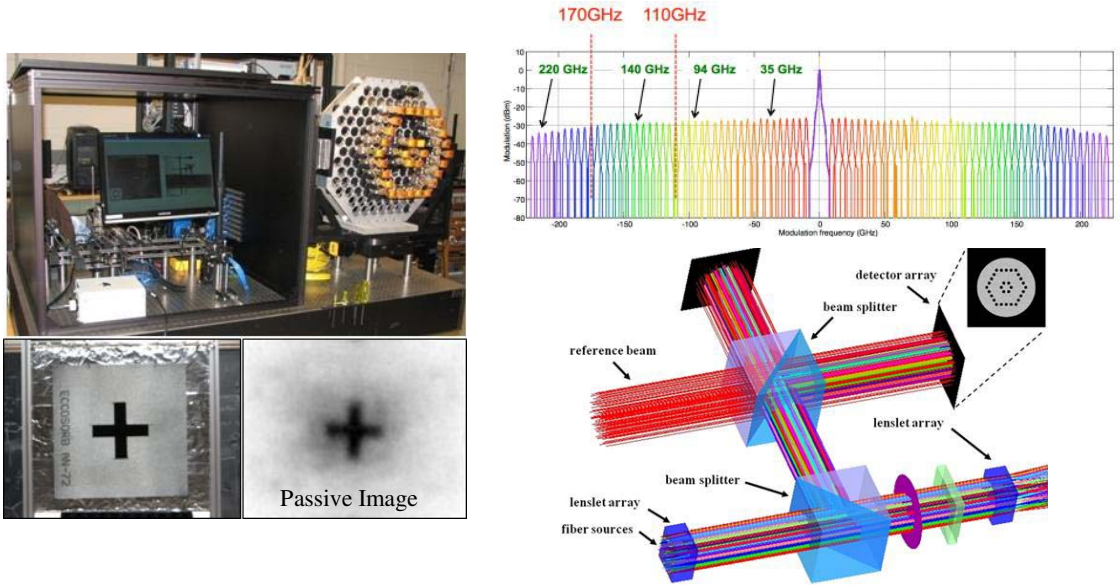

Figure 2-3: Experimentally tested and demonstrated optically addressed receiver capable of passive radiometric imagery (left), broadband optical modulators capable of E/O conversion up to 300 GHz (top right), and optical phase control system for given receiver architecture (bottom right)

Implementing the setup of spatial imaging from Figure 2-2 (top) into a usable system architecture, Figure 2-3 displays an experimentally tested video-rate receiver

based on optical upconversion. A cross was passively imaged through radiometric thermal detection using liquid nitrogen as a cold source compared to ambient temperatures. The core of these imaging systems depends on specific enabling technologies. Most importantly, broadband optical modulators are extremely essential for receiver operations. Efforts have been made to develop and fabricate ultra-broadband modulators that enable E/O conversion up to 300 GHz [19] and seen in the top right of Figure 2-3. By encoding RF energy on optical sidebands, low-loss and long-haul operation is possible while imaging the energy at the Fourier optic image plane. These devices have been heavily researched to achieve ultra low insertion loss and low half-wave voltage, V_{π}, which improves receiver sensitivity. Secondly, in order to function as video-rate receiver, image instability must be mitigated. Factors that contribute to instability include acoustic vibrations inherent to the imaging environment as well as thermal oscillations. Through a patented approach, by constructing a closed phase control loop, shown in Figure 2-3 (bottom right), we are able to compensate for the phase fluctuations in the fiber. The phase control system uses a common phase swept reference to compare each element of the fiber array against, to determine the relative optical phase of the carrier on an array of discrete detectors, Figure 2-4 (middle). The sweep results in a sinusoidal beat tone, which is digitally measured using a timing scheme in a custom programmed FPGA, as pictured in Figure 2-4 (right) and provides a DC feedback signal to each phase modulator in the array, as shown in Figure 2-4 (left). Doing so, phase variations induced in the fiber network can be compensated, resulting in stable optical processing [20]. The phase control board is also capable of powering on and off LNAs in the system for various performance metric testing and phase swept calibrations of each channel.

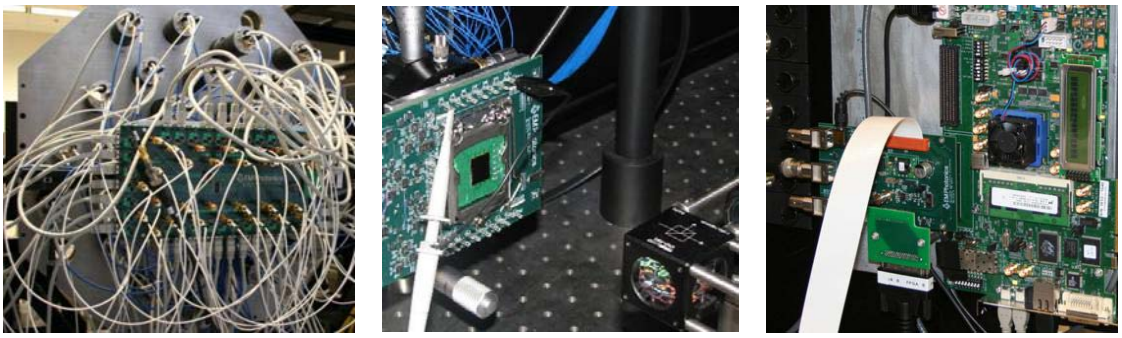

Figure 2-4: LNA power and phase control board attached to antenna array (left), FPA receiver board for phase control (middle), and FPGA for system control (right) [17]

To mitigate grating lobes associated with the sparsity of the antenna array, we transitioned from a periodic hexagonal pattern to an aperiodic array. The modification to an aperiodic structure helps diminish "mirror" images formed in passive imagery. This passive millimeter-wave receiver consists of 30 channels, operating at 35 GHz built entirely of commercially available components. A characterization of the effects of sidelobes to our imaging receiver is shown in Figure 2-5. It is evident from the PSF Sidelobe distribution graph that the maximum sidelobe suppression achievable in our system is 20%, or roughly 7 dB. Figure 2-5 (top left) shows the improved aperiodic antenna pattern to reduce the sidelobe energy. The corresponding point spread function (PSF) signifies the power spread of an RF emitter on the receiver. Unfortunately, the porous sidelobe suppression causes unwanted energy on the detector port at different degree offsets from the on-axis position. This means that adding multiple sources in the scene may not be as spatially resolute without placing them within the nulls of each transmitter's PSF. The right image of Figure 2-5 demonstrates a simulated video-rate image of a truck and a car. Since the operational frequency is 35 GHz and only 30 channels, the resolution is too poor to determine the

exact objects in the scene. Efforts have been made to upgrade the total channel count and operational frequency for more resolvable imagery [21]. In order to determine the objects in the scene, diffraction efficiency plays a major role in angular resolution. However, 30 channels equates to only 8% diffraction efficiency. While this poor diffraction efficiency is barely desirable for a communication receiver, where we want the best spatial isolation performance for multiple emissions, this receiver provided a feasible proof of concept system for testing within the PSF nulls of the transmitted signals to achieve high sidelobe suppression.

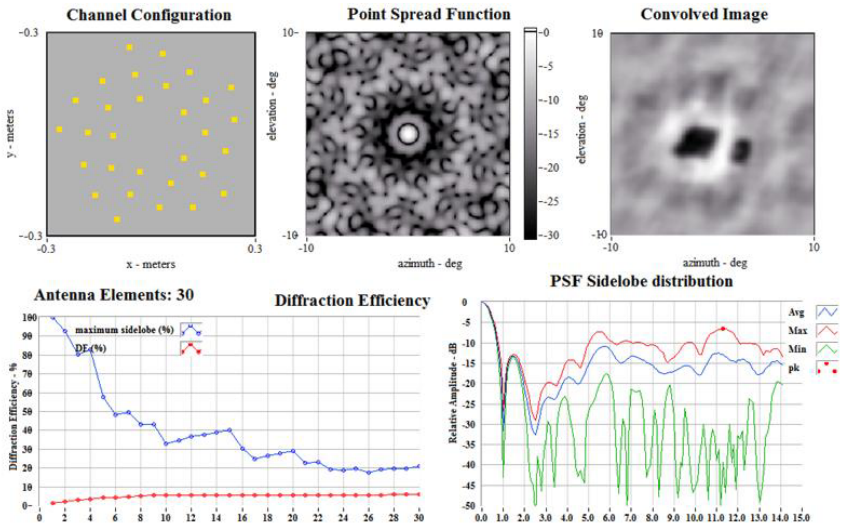

Figure 2-5: Channel configuration of the antenna array (top left), corresponding PSF of the array (top middle), and passive image of cars set at 50 meters from the receiver (top right). The sidelobe levels at radial offsets from the center of the PSF (bottom right) and diffraction efficiency as a function of the number of elements in the array (bottom left)

In our approach, the RF scene is received via a distributed aperture array. The horn antennas determine the field of view and the original acceptance bandwidth of

the imaging receiver. Each individual antenna captures its view of the scene and sends the electrical signal to a low noise amplifier for added gain in the received signal. Immediately following, the amplified signal is translated to the optical domain through modulators, where amplitude, frequency, and phase information is conserved. Optical routing to the central free space processor is accomplished through lightweight, low loss, robust fiber cables. The output of each fiber is mated to the fiber array, which is a scaled replica of the antenna array. In free space, phase compensation is completed as detailed above. Using simple optics to perform a Fourier transform of the passed through sidebands yields a reconstructed image of the spatially collected RF scene, as displayed in Figure 2-6. In this fashion, an optical camera can be used to convert the optical energy back to a resolvable image based on the preservation of the phase and amplitude information.

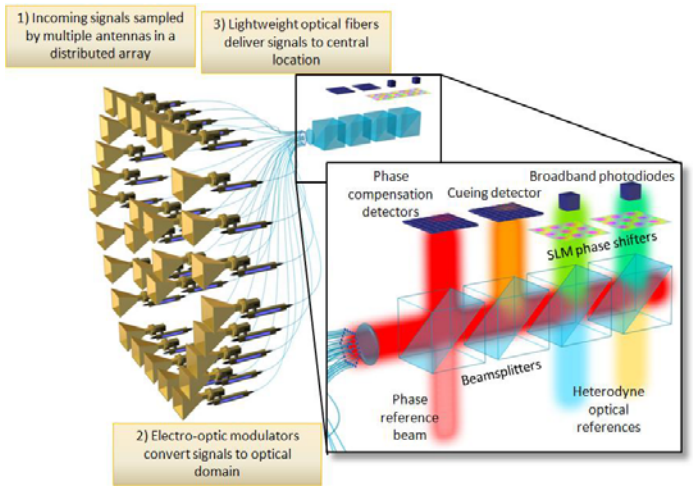

Figure 2-6: RF receiver concept to receive RF, upconvert RF onto an optical carrier, and route and process the signals via a back-end optical processor for temporal and spectral analysis.

2.2 Implementation of Signal Recovery into Receiver for Active Detection

Upon detection of RF radiation, the same optical processor is capable of electronic emission detection. Through our approach, this is accomplished by recombining the resolved emissions from the cueing detector with the source laser offset by the received frequency and directly mixed onto a high-speed photodetector. As shown in Figure 2-7, by introducing an optical beam-splitter in the path of the camera, we are able beat recovered spots with tunable optical local oscillators to downconvert the signals directly to baseband for simplistic electronic analysis. Given phase steering capabilities associated with the imaging array, we are able to image the RF scene to steer spatially filtered signals to detectors to create independent non-interfering receiver channels.

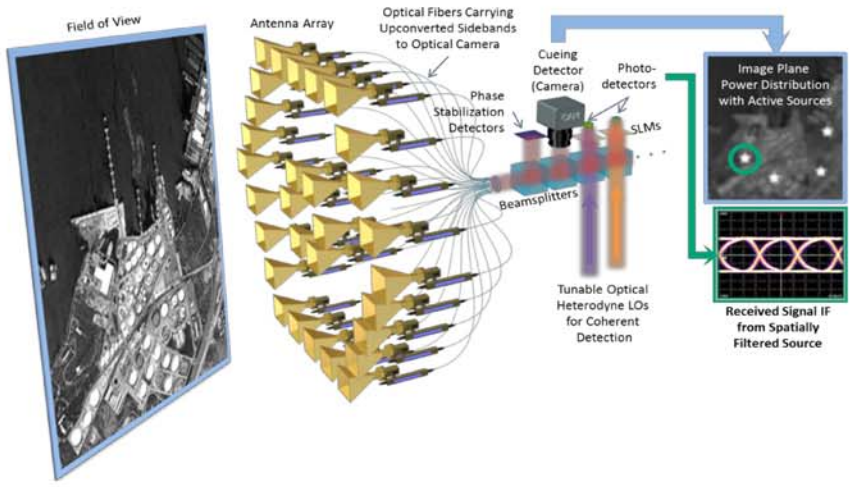

Figure 2-7: Illustration of the ability of the proposed communication receiver architecture. Spatially isolated RF sources are separately tracked and detected in the image plane and routed for IF detection

To better optimize the central processing unit for passive and active imagery, we built the setup on an optics bench. Figure 2-8 displays the optical processor layout

for our receiver approach. Here, the optical path for the carrier, sideband, and phase reference are labeled. Using a carrier beam tap, we are able to split the fiber array beam to the SWIR camera as well as the FPA board for phase control. In Figure 2-8 (left), we used a fiber free space coupler bought from Thorlabs for initial performance testing. Implementing a free space photodetector with mixed optical strength of an LO, we were concerned with LO leakage to the SWIR camera causing saturation on the detectors. Instead, optical coupling ensued in a 2x1 in-line fiber coupler where the output of the fiber coupler mated with a 40 GHz U^2T photodetector. However, due to numerical aperture mismatch of the free space coupler and the FC/PC fiber, considerable loss is experienced, approximately 20 dB. We send the recovered energy to an additional EDFA to compensate for the loss through coupling. Nonetheless, as this improves our signal strength of the optical sideband, it also proves detrimental to our noise figure and RF noise floor. To limit the amount of noise introduced in the link by the secondary EDFA, we use a tunable optical filter capable of an ultra-narrow full width half maximum (FWHM) filter span to drop excess optical noise found outside the bandwidth of the imaging receiver.

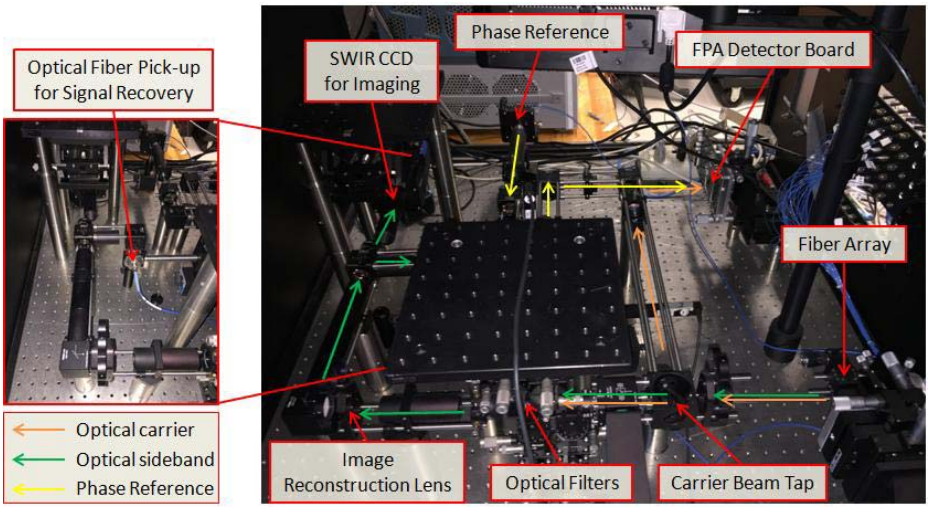

Figure 2-8: Optical processor of receiver including fiber pickup for signal recovery

Fundamental trade-offs were considered throughout the course of the research project. The major fundamental trade-off consisted of the total cost against the field of view resolution of the system. As this system was built from commercial components purchased from RF millimeter-wave and optical suppliers, the total number of elements had to remain limited to not overspend. Therefore, to optimize angular resolution to multiplex more clusters of transmitters, we would have needed to fill the antenna array completely with many more channels.

Chapter 3

OPTICALLY GENERATED RF COMMUNICATION SIGNALS

3.1 Introduction

Demand for higher data rates and congestion at the current network spectrum are the leading forces behind higher carrier frequency transmitters and receivers for next generation wireless communications [22]. As such, synthesis of radio frequency signals for the realization of radio-over-fiber systems is gaining much interest for multi-octave signal-generation [23]. Optically generated RF significantly improves the bandwidth of the system as a small shift in wavelength corresponds to a great change in frequency. A 0.8 nm shift in wavelength around telecommunication wavelengths, i.e. 1550 nm, equates to 100 GHz of usable bandwidth coverage for communications.

In order to recover the optical RF signal, an optical to electrical (O/E) heterodyne conversion on a photodetector must take place. Various photonic methods have been demonstrated to generate high-purity, tunable RF sources [24][25]. Here in, we have developed a modulation sideband injection-locked paired source capable of RF generation up to 200 GHz, limited to 110 GHz during testing due to electronic test equipment.

3.2 Design of a Tunable Optically Paired Source (TOPS)

One of the most important aspects of designing a modulation sideband injection-locked source is the ability to seed a slave laser with the appropriate amount of optical power derived from the master laser. In this case, the generated RF source is

the frequency offset between the master laser and the slave laser peak frequencies. However, seeding a slave laser at ultra-high frequency offsets above 80 GHz is extremely difficult. Typically, this requires sufficient optical input to the modulator or significant amplification after the modulator to achieve weak sideband injection-locking.

In previous modulation sideband injection-locked systems [23], a phase modulator and two DWDM filters were used to produce the sidebands for injection locking, but only the upper sideband portion. Lower sidebands were thrown out wasting the available frequency spectrum. Although efforts have been made to improve the configuration of the optical RF source by replacing a phase modulator with an intensity modulator for carrier suppression [26], half of the sidebands remained unused. To this extent, we have designed a tunable optically paired source (TOPS) utilizing two slave lasers to injection lock to both the lower and upper sidebands from the master laser. Our configuration of a dual slave laser, RF generation system is depicted in Figure 3-1. Rather than generating the frequency offset between one slave laser and the master laser, we suppress the master laser well below the first order sideband harmonic and generate the RF by the frequency separation of both slave lasers. As such, by continuously locking to the same harmonic offset from the carrier, we double the output frequency compared to previous systems. Hence, RF frequencies up to 200 GHz can be easily generated. Now, widely tunable, ultra-high data rate communication signals are possible to avoid spectrum congestion and further improve the overall network capacity.

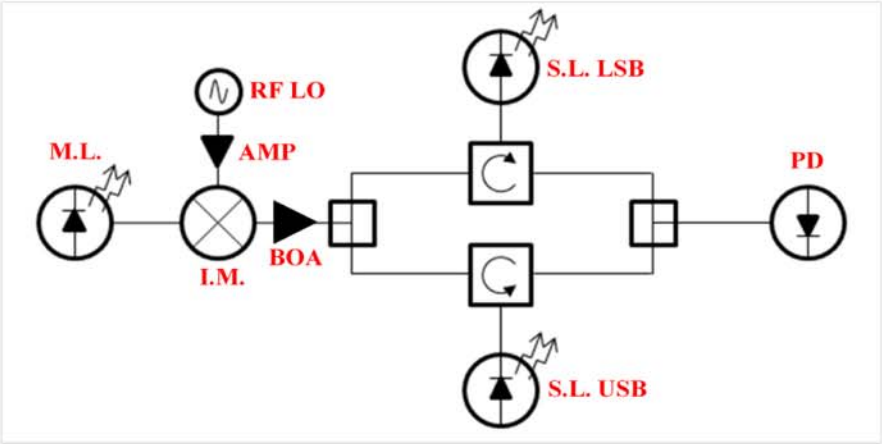

Figure 3-1: TOPS schematic with labeled photonic and electronic components

For proof of concept, a 3U (16.60 x 18 x 5.25") rackmount system was designed to hold and maintain all of the components inside, evidenced by Figure 3-2. Previous work has been made to develop small form factor, low cost TOPS systems [27]. Photonic components required for this system are discussed in the following section.

Figure 3-2: Top view of 3U rackmount chassis with included parts.

Seeding a laser for injection locking follows specific dynamics. R. Adler derived an equation in 1946 to model the effects of injection locking. He obtained a differential equation which states when a free running oscillator is perturbed by an AC injection signal, the lock dynamics are given by [28],

$$\frac{d\Delta\phi(t)}{dt} = \Delta f_0 - \frac{V_i}{V}\frac{f_0}{2Q}\sin(\Delta\phi(t)) \tag{3-1}$$

where $\Delta\phi(t)$ is the associated phase difference. The peak amplitude of the AC injection signal is given by V_i and the free running oscillator amplitude is V. The free running oscillator emits at a frequency of f_0 while the frequency difference between the oscillator and the injection locked signal is noted as Δf_0. When the free running oscillator is locked to the injected signal, the signals become coherent causing the phase difference to drop, simplifying (3-1) to an easier equation to solve

$$\frac{\Delta f_0}{f_0} = \frac{1}{2Q}\frac{V_i}{V}\sin(\Delta\phi(t)). \tag{3-2}$$

From (3-2), the sine term has to lie between +1 and -1, resulting in

$$-\frac{1}{2Q}\frac{V_i}{V} \le \frac{\Delta f_0}{f_0} \le \frac{1}{2Q}\frac{V_i}{V}, \tag{3-3}$$

further simplifying (3-3) to give the locking range f_L as

$$\begin{aligned} f_L &= 2\left|\Delta f_0\right|_{\max} \\ f_L &= \frac{f_0}{Q}\frac{V_i}{V}. \end{aligned} \tag{3-4}$$

It is evident that a free running laser has twice the frequency differential locking range given by either side of the frequency spectrum of the injected signal. By understanding

Adler's equation, we are able to maximize the locking range of our TOPS slave lasers. Figure 3-3 displays the locking range of our system around 10 GHz. From the Figure, a 4 GHz locking range was achieved by maximizing $\frac{V_i}{V}$, while maintaining high oscillator amplitude, V. Since we injection lock to two slave lasers, our corresponding f_L is 2 GHz per oscillator. In comparison, other work designing such modulation injection-locked sources has demonstrated much worse locking ranges [29]. While a larger locking range is unsuitable for low frequency generation, below 1 GHz, the large locking range allows for added calibration error of slave laser set frequencies. Meaning, each slave laser calibration file is able to have up to 2 GHz error at each frequency before issues arise. To generate low RF frequencies, we can redesign the system to have only one slave laser turned on to lock to a harmonic offset and beat it on a photodiode from the original master carrier, rather than the second slave laser. This will allow us to generate half of the expected frequency of the current design, allowing frequencies as low as the minimum frequency generated by the RF synthesizer. In our case, a 500 MHz tone can be generated through this redesign of our TOPS, rather than 1 GHz. High frequency locking, above 20 GHz, is extremely difficult to automate RF generation without a wide locking range. For instance, 2 GHz corresponds to 0.016 nm optical wavelength separation. In order to perfectly calibrate a laser within that separation, perfect temperature stability and tunability must be possible, but not difficult. However, locking ranges on the order of 300 MHz and lower as calculated from other RF generation efforts correspond to roughly 0.002 nm optical separation of the free running oscillator to the injected signal. Clearly, maintaining optical wavelength calibrations within 300 MHz of the injected laser prove extremely daunting as ambient temperatures fluctuate.

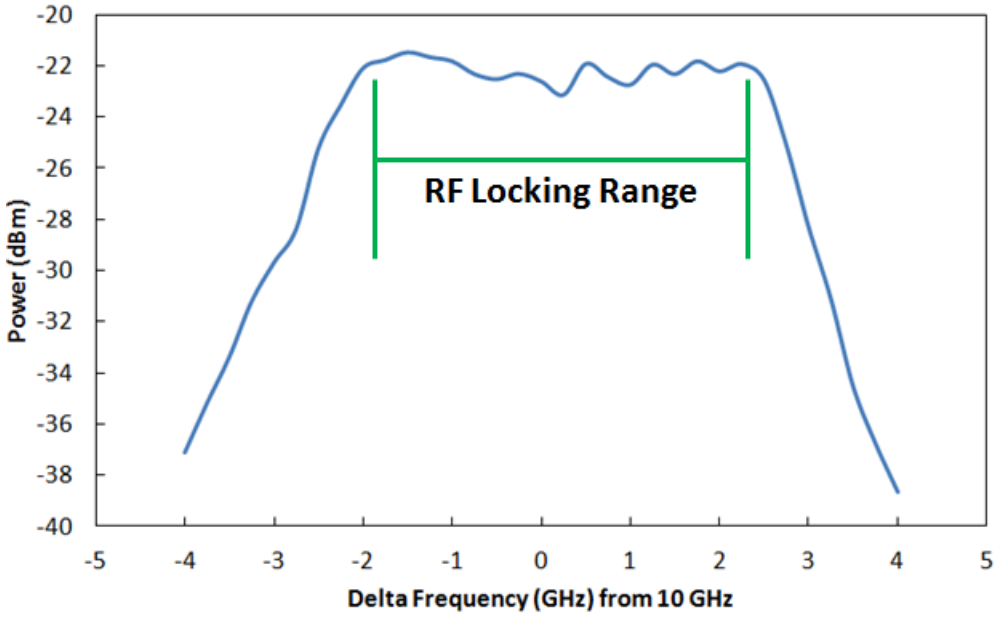

Figure 3-3: RF locking range of the TOPS offset from 10 GHz

As mentioned, generated RF frequencies above 20 GHz is difficult to maintain without a very large locking range. The TOPS communication source is capable of 100 GHz automated RF generation with continuous locking without the need to re-tune the slave laser temperature setpoints. Figure 3-4 shows the difference between the locked and unlocked signals at 100 GHz. Here, the slave lasers were automatically tuned to their respective setpoints with and without sidebands injected into their cavities. However, it is clear from the locked signal that there is noise surrounding the RF signal at 100 GHz. In this case, not all of the phase noise has been cancelled out.

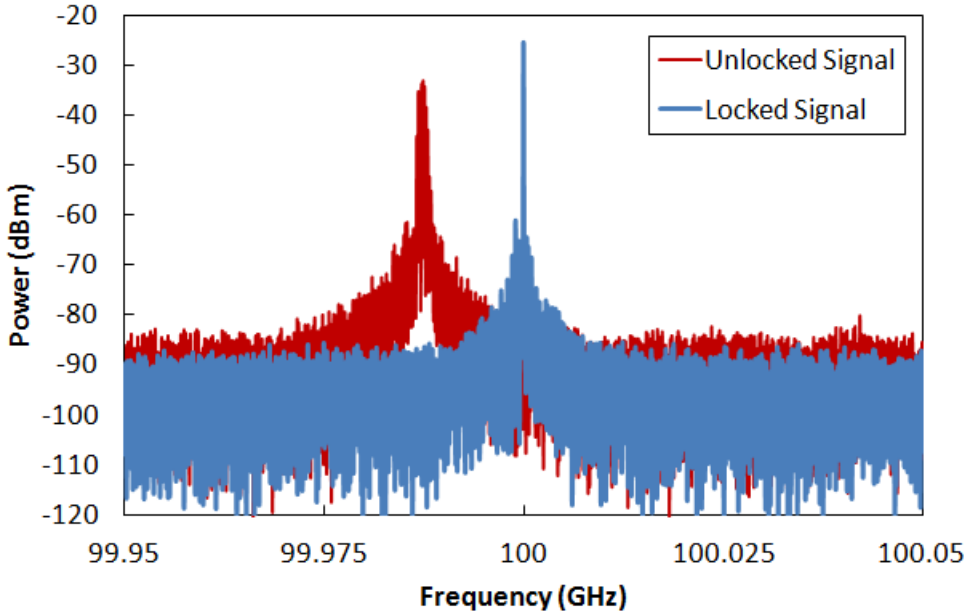

Figure 3-4: Comparison of locked and unlocked RF at 100 GHz by turning off master laser into the modulator

Phase noise has numerous dominate sources in the TOPS system represented in Figure 3-2. Scaled minimum phase noise present from the RF synthesizer is an important contributor; however, other contributors such as thermal and acoustic effects on the optical fibers, path length mismatch, and current fluctuations in the lasers also greatly affect the phase noise. The primary source of phase noise has been experimentally validated to be due to thermal and acoustic noise. As seen in Figure 3-2, all of the fibers are contained within laser temperature controllers/drivers. As the temperature changes or the fans run more rapidly, thermal and acoustic vibrations drastically affect the phase noise. Figure 3-5 illustrates the phase noise derived from the RF Synthesizer as well as the optically generated RF at 5 GHz. The vibrations and temperature variations are apparent at offsets smaller than 10 kHz. In order to further minimize the phase noise of the generated communication signal, the length of fiber in

the system should be minimized and the contained fiber should be mounted elsewhere, not in the laser drivers. Taping the extra fiber to a shelving unit would further reduce the vibrations from the fans and the temperature changes in the laser controllers.

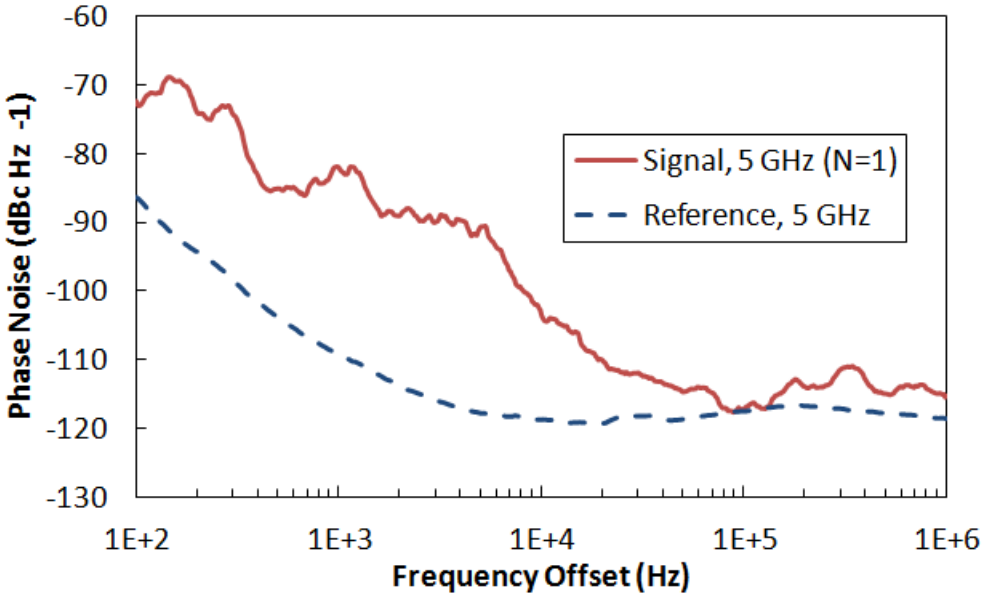

Figure 3-5: Phase noise comparison of RF synthesizer and TOPS output

High purity tones are essential to communications. RF signals with large linewidths have been shown to have extremely poor BER [30]. Most high frequency generation methods are reaching the minimum limit of achievable linewidth, which are typically observed around 100 MHz and greater [31]. However, sideband injection-locking maintains coherency throughout the system and as long as the paths are matched in both slave laser arms, measured linewidths on the order of ~1 Hz can be demonstrated over the entire frequency spectrum. Figure 3-6 demonstrates single digit RF linewidth achievable at 45 GHz.

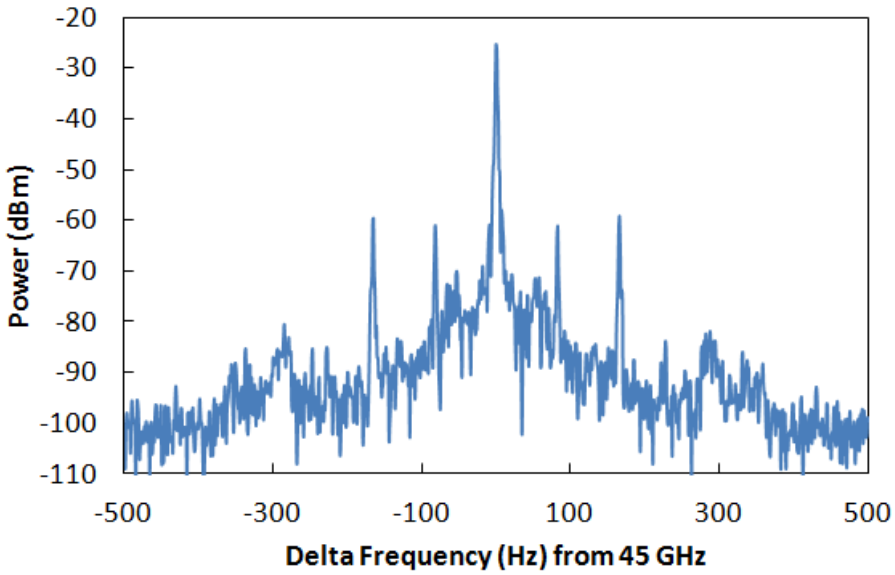

Figure 3-6: Linewidth of RF signal at 45 GHz

3.2.1 Photonic Components Required

The components in the TOPS generator are shown in Figure 3-7. To reiterate, the purpose of the components is to thermally tune two slave lasers to a specific frequency offset from each other to generate RF with ultra-wide bandwidth (UWB). The output of the modulator is split to two fiber arms and injected into slave lasers without isolators. One slave laser thermally tunes and locks to one of the injected lower sidebands, while the second slave laser thermally tunes and locks to one of the injected upper sidebands from the master carrier. As a result of the locked lasers having identical phase noise, the purity of the reference can be preserved and maintain a linewidth of ~1 Hz over the entire range of operation. As an added capability, the inclusion of a DQPSK modulator for RF I-Q transmission is possible for complex modulation formats for wireless communications. In the following paragraphs, each

component will be discussed in detail in chronological order according to the schematic of Figure 3-1.

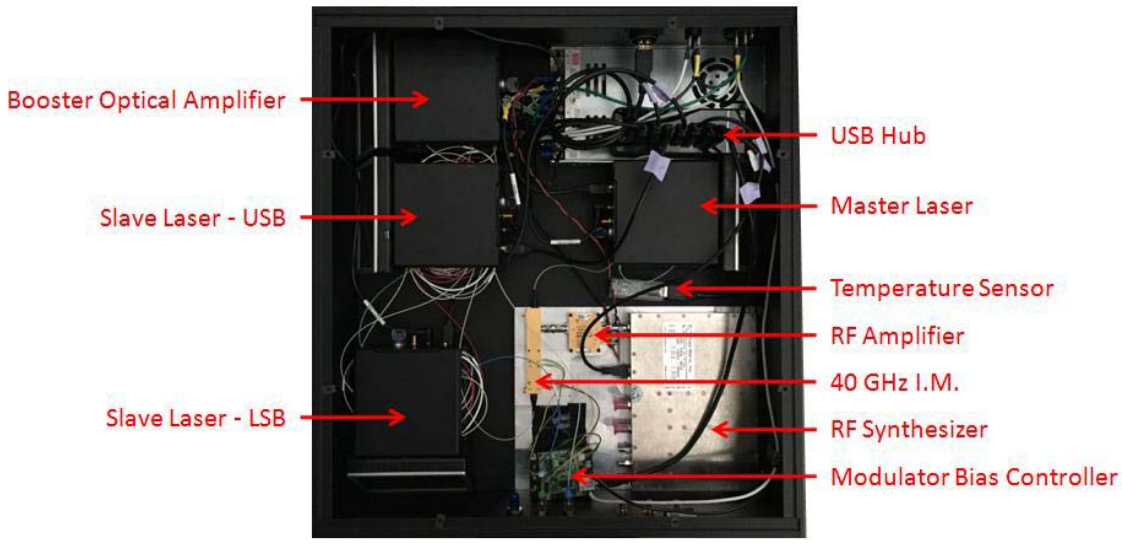

Figure 3-7: TOPS design with labeled components

The first component to be discussed is the master laser. The laser was purchased through Gooch and Housego. It is a 100 mW DFB laser in a 14-pin butterfly package (AA1406-192400-100-PM900-FCA-NA). The master laser contains an isolator to prevent back reflections into the laser cavity. Centered around channel 24 on the ITU frequency grid, the laser has the capability of being tuned by 100 GHz. Setting the laser in between the tuning ranges of both slave lasers, wideband RF generation is possible.

In order to operate the lasers, efficient controllers were required. To the best of our knowledge, Thorlabs laser drivers/temperature controllers (CLD1015) provided the most stability and most convenient LabVIEW connectivity. These controllers

offered consistent current output of the lasers while maintain exact temperature settings through TEC capabilities. By tuning the temperature of the TEC, the laser output frequency would change accordingly, about 10 GHz per 1^{o} C. In addition, these controllers came in a small form factor design that allowed them to be placed within the 3U rackmount chassis.

The next component of interest is the RF Synthesizer. This component was purchased through National Instruments (originally Phase Matrix) to act as our low frequency RF oscillator (FSW-0010). This is a full feature model synthesizer capable of tuning frequency, power, and incorporating different modulation types (AM, FM, and pulse). In terms of frequency generation, the synthesizer outputs between .5 to 10 GHz allowing frequencies as low as 1 GHz to be generated. Tuning power allows us to change the RF input to the amplifier to reduce saturation in the first order harmonic. For the purpose of generating a single RF tone, the phase noise and low-frequency stability are extremely essential to producing ultra-pure tones.

Third component is the RF amplifier. The amplifier used in the source is a high-gain 50 GHz RF Lambda LNA (RLNA00M50GA). Gain was measured to ~37 dB throughout the bandwidth of the amplifier while introducing minimal noise figure of 4 dB. This LNA was chosen due to its relatively low saturation power output; compared to the gain. The purpose of the amplifier is to operate within its non-linear range to saturate the original RF tone, but amplify all harmonics of the RF tone. This non-linear distortion acts as the basis for injecting all of the tones into the modulator for up-conversion.

The fourth component, probably the most critical, is the optical modulator. The modulator used is a high extinction ratio (HER) intensity modulator from Optilab (IM-

1550-40-PM-HER). With a 45 GHz bandwidth, optical modulation at high order harmonics is possible. However, in order to lock to low frequencies, the first sideband harmonic must be greater in optical power compared to the carrier. Using this HER modulator, we experienced over 25 dB carrier suppression at its null bias point.

In order to achieve large carrier suppression, a modulator bias controller was required. The purchased bias controller is a YYlabs Mini-MBC-5 (product number 0045). It works by sweeping voltages across the modulator bias pins and detects the power read by a photodiode accordingly. One major benefit of MBC is its ability to maintain its bias for a very long time.

Next, a booster optical amplifier (BOA) is used to amplify/attenuate the optical sidebands. The BOA was purchased through Thorlabs (BOA1004P). After the modulator, optical power of the low order harmonics (1-4) must be attenuated in order for the slave lasers to weakly lock appropriately. For higher harmonics, the BOA current will slowly begin to increase its gain output for greater sideband amplification.

The last two essential components to the TOPS generator are the two slave lasers. Both lasers were purchased through Gooch and Housego. The lower sideband slave laser (AA1408-192400-100-PM900-FCA-NA), is a 100 mW DFB laser in a 14-pin butterfly package. The upper sideband slave laser (AA1408-192300-100-PM900-FCA-NA) is also a 100 mW DFB laser in a 14-pin butterfly package. Both lasers lack an isolator into the laser. This is required for the sidebands to seed the laser cavities. The lasers are capable of being tuned 100 GHz centered on their specific ITU frequency channel in order for UWB injection-locking.

3.3 High Frequency Performance and Characterization

A number of properties are significant for the implementation into wireless communication networks, but spectral coverage is the most significant. Large spectral coverage offers greater data capacities before the bandwidth shortage becomes more apparent [32]. In the below Figure, Figure 3-8, we illustrate the ability of our TOPS to generate pure RF tones from 1-100 GHz. Each signal was recorded via a custom automated frequency sweep program designed in LabVIEW. Output power fluctuations can be attributed to slight current instability in the slave lasers as well as changes in the RF spectrum analyzer during data acquisition. Our Agilent N9030A spectrum analyzer operates up to 50 GHz. Data recorded from 1 to 50 GHz was taken directly from the RF input to the analyzer. In order to detect RF above 50 GHz, external mixers were necessary to increase to detection frequency range. Unfortunately, our calibration mixer in V-band (50-75 GHz) had communication issues prohibiting analyzer connection. As a result, frequencies within V-band were ignored for the purpose of this sweep. However, provided generated RF was achieved in W-band (75-110 GHz), no issues are expected to cover the entire spectrum. The output of the slave lasers were mixed on a 100 GHz U^2T photodetector (XPDV4121R). As stated earlier within the Chapter, this is a dual slave laser adaptation of an existing tunable source that achieved 100 GHz using a single slave laser. Extracting injecting locking strength at ultra-high harmonics from the master laser, we expect generated frequencies to double our current recorded data. Meaning, up to and exceeding 200 GHz RF should be achievable, but electronic mixers cannot reach such high frequencies. To determine injection-locking above 110 GHz, an optical spectrum analyzer can be utilized with slight concerns about its minimum

resolution BW of 0.01 nm, which corresponds to roughly 1.25 GHz resolution. Using an optical spectrum analyzer would alleviate the need of a high frequency photodiode.

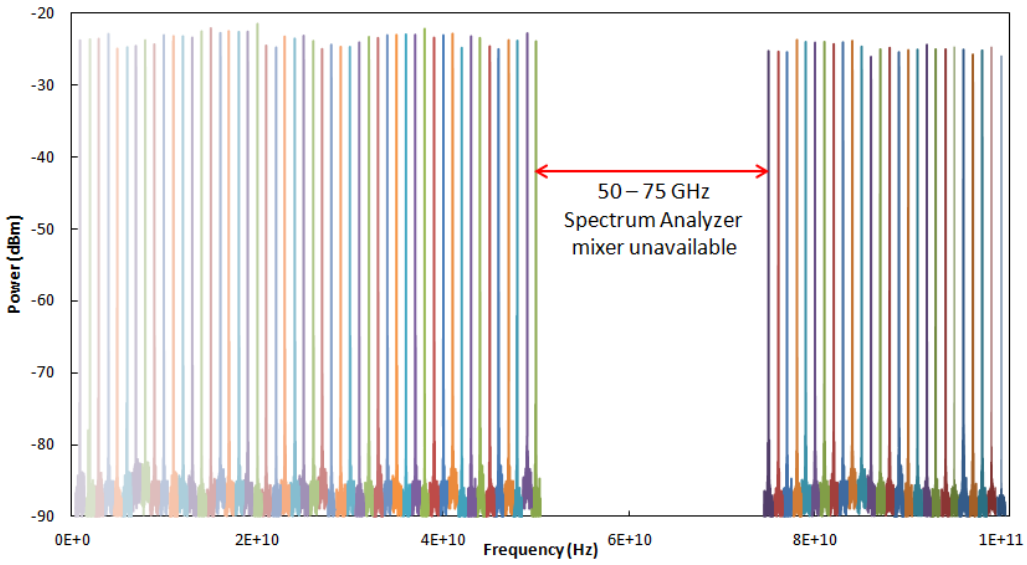

Figure 3-8: RF spectrum of generated RF from 1 to 100 GHz using TOPS

A growing concern with injection-locked sources is the RF generation from the unused sideband harmonics. As higher frequencies are generated, the optical power of the lower harmonics increase proportionally with the BOA, generating RF tones at high output powers. Efforts are currently being investigated to incorporate narrowband tunable optical filters after the BOA, but before the split to the individual slave lasers to pass only the sideband of interest for pure RF generation. In doing so, we are able to replicate a microwave generator at significantly higher frequencies than realizable through electronics.

Chapter 4

INITIAL IMAGING AND DETECTION RESULTS

4.1 Single-Source Detection using a single TOPS Source

Spatial multiplexing of the RF scene is crucial to frequency identification and demodulation of communication signals. Angle-of-arrival places incoming signals at spatially separate locations in the image plane. In order to optically detect emitted frequencies, we paired the RF receiver discussed in Chapter 2 with a high-speed photodetector at the same image plane of the cueing detector. Considering our receiver as a wireless network base station, we wanted to determine the full capacity to image the passive scene while detecting active transmitted sources. To begin, the TOPS source was set to operate within the acceptance bandwidth of the imaging system. Figure 4-1 (left) depicts a millimeter-wave image of the detected passive and active field of views. Although the imaging receiver has sufficient sensitivity for capturing passive radiometric energy, the high noise figure associated with the current LNAs of our receiver cause less than resolute passive imagery due to the NETD of the system. A can containing liquid nitrogen (LN) was used as our passive imaging object and can be seen on the left side of Figure 4-1 (left) where black represents cold temperatures. Aliasing is evident as the LN object appears to be behind the transmitting source as well. Passive imagery involves detecting blackbody radiation given off by the RF scene at all frequencies, described by Plank's equation:

$$I(\upsilon,T)=\frac{2hc^2}{\lambda^5}\frac{1}{\exp(\frac{hc}{\lambda kT})-1}. \tag{4-1}$$

Blackbody radiation contains the temperature information of the entire scene as well as the frequency information as found in the exponential in (4-1). Colder objects act as a lack of emitted blackbody radiation. As such, the radiometrically cold sky provides the greatest temperature difference, however, working in a lab, we matched the temperature of the cold sky with LN. Placed to the right of the LN can was a TOPS generator attenuated to an output power just above the noise equivalent power (NEP), nano-Watts, of the system. Both the LN can and the source were stationed three meters from the receiver. During testing, we routed the high-speed photodetector to an electrical signal analyzer (ESA) for frequency identification to determine the validity of our RF receiver approach. Figure 4-1 (right) illustrates the spectra of the detected bright spot in the image which originated from the emission of the TOPS transmitter.

At the photomixing process, homodyne detection was performed since the two fields for the received sideband and the master carrier originated from the same source. Both fields can be described as

$$e_s = E_s\cos(\omega_s t+\phi) \tag{4-2}$$

and

$$e_c = E_c\cos(\omega_c t) \tag{4-3}$$

for the sideband and the master carrier, respectively. Here, E_s is the amplitude of the optical sideband and ω_s is its angular frequency. Similarly, E_c is the maximum amplitude of the master laser and ω_c is its angular frequency. For homodyne

detection, the frequency offset of the two optical signals corresponds to the generated RF output frequency, such that:

$$\omega_{RF} = \omega_c - \omega_s \tag{4-4}$$

and the corresponding current output of the photodiode is

$$I_{PD} = \frac{2\eta e}{hf}\sqrt{E_s E_c}\cos(\omega_{RF}t + \phi), \tag{4-5}$$

resulting in an RF power, P_{RF}, of

$$P_{RF} = \frac{1}{2} {I_{PD}}^2 R, \tag{4-6}$$

where R is the resistance of the device, typically measured as 50Ω.

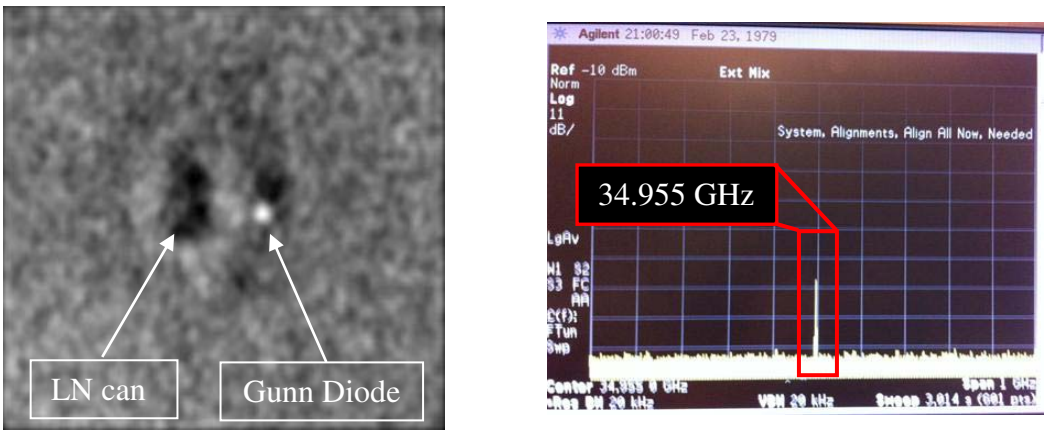

Figure 4-1: Image from 35 GHz passive millimeter-wave imaging system showing both passive and active field of views from three meters away (left) and the mechanically tuned Gunn diode detected on an RF spectrum analyzer (right) [20]

4.2 Multi-Source Detection

As imperative in the communications environment as it is to detect a single mobile device or route the received energy, in most practical cases, more than one communication transmitter will be evident within each BSs field of view, especially adjacent channel and co-channel sources. This causes the BSs to identify more than just a single frequency cell on the photodetector to cover a certain geographical area [33]. To prove this capability, we placed two TOPS driven RF sources in the imaging scene to demonstrate the possibility of MIMO reception. MIMO systems offer dramatic data throughput gains compared to SIMO systems since each signal experiences spatial freedom from all others for interference cancellation [34]. Figure 4-2 shows the experimental setup (left), as well as the RF spectrum analyzer data (right), which proves that this imaging technique can recover all of the sources in its scene, albeit, not capable of identifying the spatial positions of the signals compared to their bright spots on the simple CCD detector. This is attributed to the detector port not perfectly stationed to match the image plane of the CCD camera. As a result, sidelobe energy became the dominate factor in recovering RF radiation.

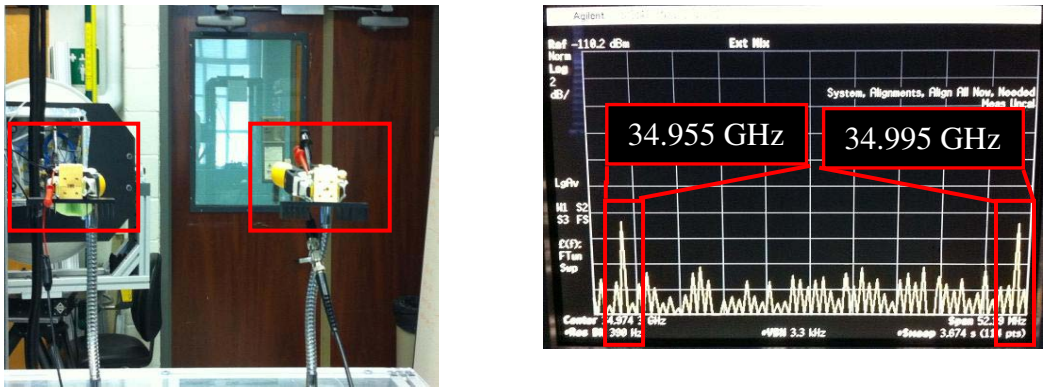

Figure 4-2: Image of two sources (left) and the received RF Spectrum (right) [20]

4.2.1 Spatial Separation Results

To demonstrate the full capability of our optically enabled receiver architecture, we mounted the free space coupler to a 2-axis motion controller to continuously calibrate the center spot of the detector to match that of the cueing detector. In order to do so, the output of the coupled fiber went to an optical spectrum analyzer where we translated our detector port until we experienced a maximum power at the image plane. To ensure proper calibration, we phase steered the receiver away from the imaged source to confirm power roll-off equivalent to that of the PSF sidelobe suppression. After optimization, we preformed the same two-tone emission demonstration of Figure 4-2 once more, but with the additional ability to spatially isolate incoming signals, as indicated in Figure 4-3 below. In order to spatially isolate each emission individually, we needed to steer the imaging receiver to focus solely at one emitter at any given moment. Our view of MIMO detection is skewed to the extent that we use a single photodetector, creating more of a MISO system allowing us to detect specific singular emissions. Beam steering was accomplished by applying the

appropriate phase shifts to the output of the modulators in the antenna array. As a result, we were successful in demonstrating that our receiver could be steered to a specific signal of interest onto the detector for improved SNR and dynamic range while in the presence of an adjacent channel. For early RF analysis, we were able to prove our communication receiver approach could mitigate ACI with sufficient sensitivity.

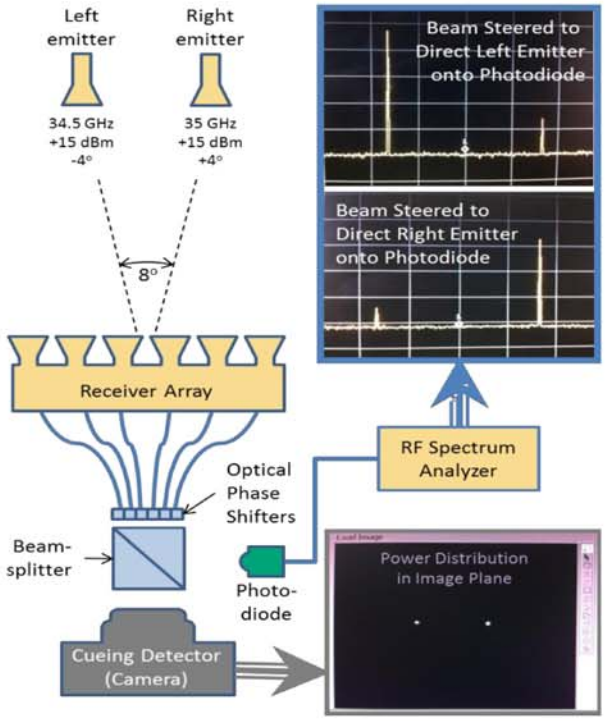

Figure 4-3: Illustration of preliminary demonstration of spatial multiplexing discrimination by the proposed receiver configuration

The spatial isolation of the imaging system can be best described as human vision. As one begins to focus on an object, say object A, all other objects directly surrounding object A remain apparent. However, objects outside of the focus cone of

the person's eye sight, begin to blur, much like the second source outside of the angular resolution of the system. As the person now shift their attention to on object B, rather than object A, object B becomes more clear, while object A falls into the peripheral vision of the human and begins to blur. As such, this compares to our receiver phase steering to a specific individual RF emission while all others fall in the peripheral of the detector, where sidelobe energy in dominate. Minimal energy is still apparent within the detector for those signals, however, recognized at orders of magnitude below the signal of interest. This is the capability of our phased-array receiver. The spectra shown on the right on Figure 4-3 were both acquired with the detector in the same position. No mechanical movements were made in the system, only voltage adjusts to the modulator's DC phase port.

4.3 Beam-Steering Power Characterization

Although spatial multiplexing is crucial in discerning communication signals in the field of view of the BS, the efficiency at which the receiver can steer each incoming signal to its own detector and distinguish all the cells within close proximity to each other is far more valuable to improving wireless network capabilities. Without the ability to discern closely emitting signals, CCI and ACI become ever more dominant.

Since our 2D phased-array receiver approach has the capability of steering in both azimuth and elevation directions by 0.1 degree increments, we wanted to characterize the overall angular resolution, spatial isolation, and efficiency of our receiver to accurately detect and locate multiple signals by directing the steered energy onto the photodetector. Angular resolution is the minimum angular separation between

two equivalent sources at the same range away from the BS in order to accurately detect both separately, and is described as:

$$\sin\theta = 1.22\frac{\lambda}{D}. \tag{4-7}$$

Here, λ corresponds to the operational wavelength of the imaging receiver, i.e. 35 GHz, and D is the diameter of the antenna aperture. Substituting our values of 8.56 mm for λ and 0.6 m for D, we get $\theta = 0.997^{o} \approx 1^{o}$. For wireless networks, the smallest θ possible offers greater network coverage, improving consumer capacities.

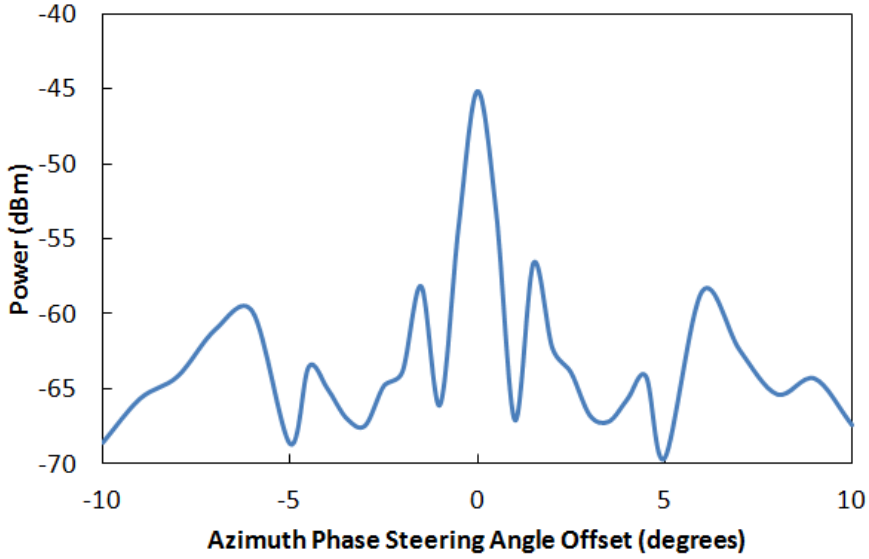

Figure 4-4: Power detection through phase steering in Azimuth direction

Data was recorded from a single TOPS generator set 1.6 meters from the imaging receiver. At 1.6 meters, we were able to fill the entire antenna aperture with the incoming signal with minimal directivity loss according to both transmit and receive antennas. Initial characterization was taken in the azimuth direction and can be shown in Figure 4-4. Tracing the max power to its first null at either degree offset, it is

apparent the roll-off is observed at ± 1 degree offsets matching the angular resolution calculated above. Observed at the null point was a 20 dB mainlobe power suppression. Fluctuations in RF power throughout the phase steering sweep can be attributed to RF sidelobe power as simulated in Chapter 2. Improving sidelobe reduction requires an increase in antennas within the aperture. A 20^{o} sweep at 1.6 meters equates to a 23 inch total distance sweep. Within the 23 inches, the mainlobe was isolated to a 2.2 inch location.

Likewise, an equivalent 20 dB power suppression was observed on the photodetector during phase steering in the elevation bearing from ± 1 degree offset from the mainlobe angle, as seen in Figure 4-5. It is clear the first null point in positive, upward, offsets is much greater than in negative, downward, offsets. This can attributed to inconsistent power uniformity across the array. Elevation steering resulted in an isolation of 2.15 inches compared to the 23 inch sweep. Maximum RF power differentiation from the mainlobe to the maximum sidelobe is roughly 10 dB. With a partially populated antenna array, we are only able to achieve such poor sidelobe suppression. However, the order of magnitude suppression offers enough suppression in SNR to decipher each co-channel or adjacent channel signal within the cluster resolution.

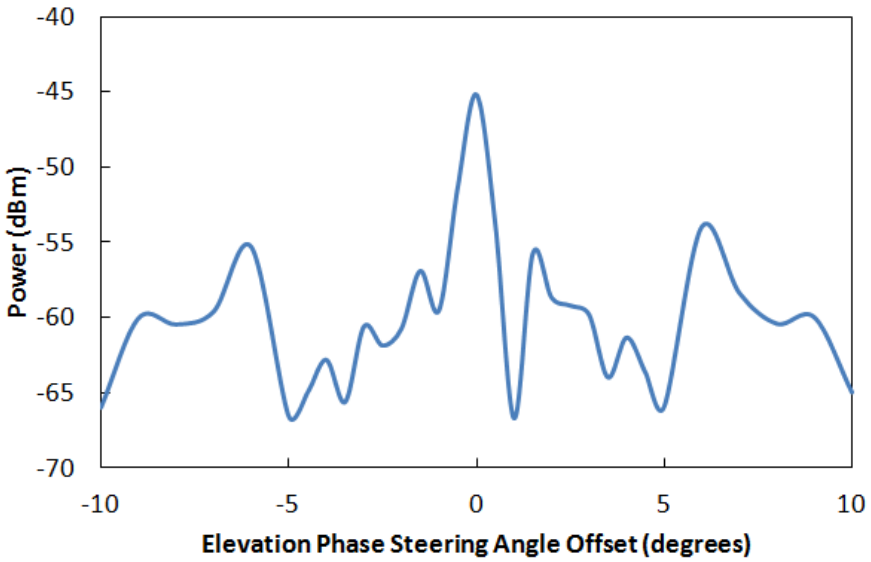

Figure 4-5: Power detection through phase steering in Elevation direction

Provided consumer usage continues to grow, BSs will need to spatially multiplex clusters of cells to determine the transmitted information. Investigations into geolocation of cells compared to angular separation offer insight to the overall efficiency of our BS receiver. Two specific spatial distances were taken into consideration for determining the effectiveness of our communication receiver: close proximity to the receiver and each cell as well as broad separation of cells to the BS. Figure 4-6 (a) graphs the detect reading of two TOPS generators, set to RF outputs of 35 GHz and 35.5 GHz, respectively. Power readings were taken on an electrical spectrum analyzer at 0.5 degree intervals ranging from -5 to 5 degree offsets from on axis bearing. The sources were placed 1.6 meters from the imaging system and separated by a measured distance of 2.55 inches, as shown in Figure 4-6 (b). The experimental separation determined by

$$D_S = d * \tan(\Delta\varphi), \tag{4-8}$$

where d is the fixed distance from the imaging receiver and $\Delta\varphi$ angular separation of the maximum points for both lines. For close proximity, $\Delta\varphi$ was determined to equal 2.6°, resulting in D_S of 2.86 inches. The 0.31 inch error value corresponds to a 12.2% error in separation distance. This error can be attributed to angular resolution of the system creating an appearance of the two sources blurring together. Another contributing factor is the presence of sidelobe power interference convoluted onto the photodetector. Unfortunately, sidelobes cannot be factored out as they are fundamental properties of the antenna radiation pattern. With that being said, regardless of error contributors, it is evident that both emissions have recognized maximums at separate locations in space.

Second experiment consisted of backing the sources away from the imaging receiver to 4.3 meters and spacing the signals to a measured separation of 33 inches as seen in Figure 4-7 (b). Again, RF data was documented from the electrical spectrum analyzer for a 20 degree span of 0.5 degree intervals, as shown in Figure 4-7 (a). A 20° azimuth directional steering corresponds to a 61.6 inch steering length across the scene. Experimental calculations produced a $\Delta\varphi$ value of 11 degrees. Factoring in the angular separation into equation 4-7, we get a separation distance, D_S of 32.9 inches. The 0.1 inch error value corresponds to a 0.3% error in separation detection. Almost zero percent error is contributed to the suppression of sidelobe power detected on the photodetector as well as the spacing between signals is much greater than the angular resolution of the system.

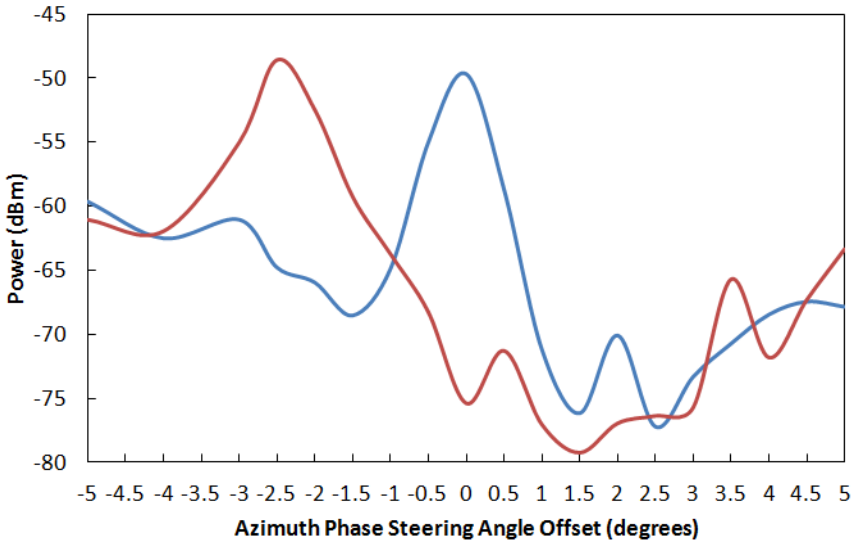

(a)

(b)

Figure 4-6: Power detection of two closely spaced sources transmitting from 1.6 meters from the imaging receiver (a) and visual image of sources taken from standard camera mounted in the center of the antenna array (b)

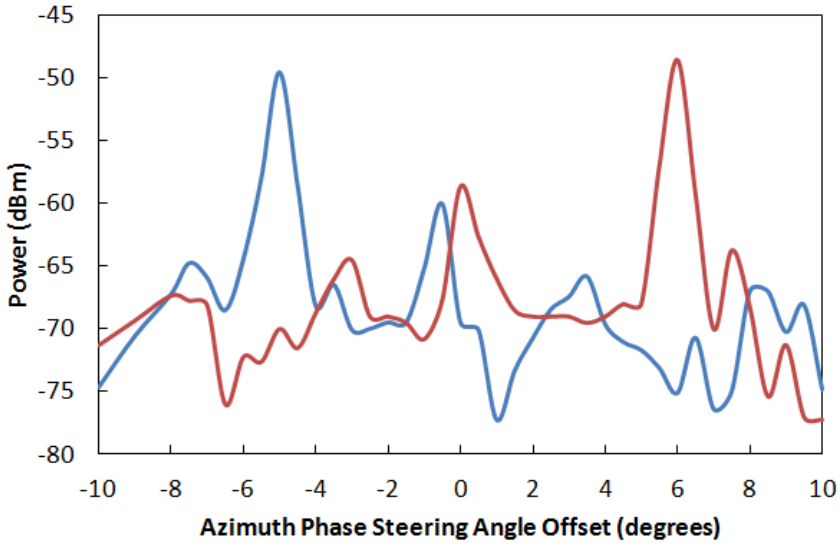

(a)

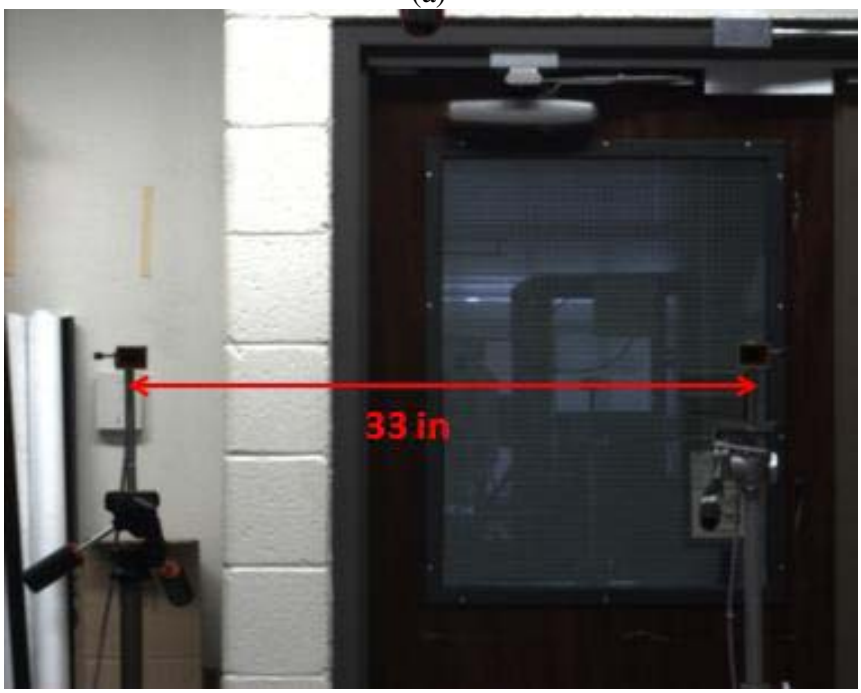

(b)

Figure 4-7: Power detection of two widely spaced sources transmitting at 4.3 meters from the imaging receiver (a) and visual image of sources separated by 33 inches (b)

Results confirm that our communication receiver has the potential to be a very efficient approach for spatial multiplex capabilities required for wireless networks. Factors contributing to error can be simply improved by narrowing the angular resolution and suppressing sidelobe power. Angular resolution can be improved by increasing the operational frequency of the receiver or increasing the aperture size of the receiver. Fully populated arrays will help with sidelobe reduction.

Though these demonstrations of signal recovery and analysis shows promise of implementation for communications, the direct recovery of signals at high frequencies, i.e. 35 GHz, incurs major SNR limitations. Millimeter-wave frequencies place a great deal of limitations on photodetectors. First, millimeter-wave frequency photodiodes are very costly. High-speed photodetectors require small active regions to operate. This places limits on the maximum photocurrent they can handle, ultimately reducing the dynamic range and SNR performance of the receiver. The small photodetector diameters also introduce added burden on optical coupling of the recovered signals onto the photodiode, consequently, incurring major coupling losses via fiber based couplers or direct free space lens setups to the photodiode. In most cases, digitizing technologies are limited by the ADC converters at high frequencies which require RF downconversion to baseband anyway for communication operations. Thus, we needed a means to generate and mix the received signals to baseband optically. As a result, we developed a technique to mix the spatially isolated signals with an injection-locked optical local oscillator to grant direct downconversion to an intermediate frequency upon photodetection. Through heterodyne detection to IF, high-power, improved SNR operations are possible through low speed photodetectors. The design and implementation into our receiver approach is described in the following chapter.

Chapter 5

IF GENERATION THROUGH OPTICAL DOWNCONVERSION

5.1 Introduction

The purpose of an optical local oscillator (LO) is to set a secondary laser to a specific frequency offset from an original laser source to generate a new output frequency [35]. Thus, in our approach, this is accomplished by photomixing an injection-locked laser with the received energy from the communication receiver on a high-power, low-speed photodiode (PD) for downconversion to an appropriate intermediate frequency (IF). In addition, by utilizing a high-power LO, superior RF outputs are achievable. Injection-locking is realized by using a broad comb of sideband harmonics, all created from externally modulating the source laser from the 35 GHz imager with a low-frequency RF reference that is subject to nonlinear distortion through RF amplification. The amplifier non-linearly adds gain to harmonic multiples of the input RF frequency. All of the multiples are then up-converted to the optical domain using a phase modulator. After optically band-stop filtering the carrier and lower sidebands, passing only the upper sideband harmonics, a second laser, or slave laser, is then thermally tuned to match and lock to the frequency of any one of the injected harmonic sidebands. The locked lasers preserve the linewidth of the reference of ~ 1 Hz.

5.2 Design and Construction of the Optical Local Oscillator

Implementing into the communication receiver, this system can function as a wideband photonic tuner. RF signals are received by the receiver, processed within the optical free-space setup, and mixed on a photodiode for heterodyne downconversion. The generated IF output signal offers numerous advantages over direct detection such as exceptional instantaneous bandwidth (IBW) and improved dynamic range. The benefit of the optical LO is that the photodiode only needs to possess sufficient speed for the IF plus the signal bandwidth. For our purposes, the LO generally is used to convert the received communication signals to baseband frequencies, meaning, we are able to use large diameter, high optical power handling photodiodes. Thus, higher SNR values can be achieved through photonic downconversion.

In terms of the receiver architecture of Figure 2-7, a single (master) laser is amplified and divided into 32 fibers. As previously mentioned, there are only 30 antennas in the system requiring each to have a fiber used as the input to the electro-optic modulator, leaving two fibers unused. Taking one of the unused fibers, we are able to generate coherent heterodyne optical local oscillators [36]. A schematic shown below in Figure 5-1 demonstrates the capability to spatially recover signals from the imaging receiver and mix onto a photodiode for heterodyne conversion. At the input of the photodiode, the two fields for the recovered signal and the LO may be written as [37]

$$e_s = E_s \cos(\omega_s t + \phi) \tag{5-1}$$

and

$$e_L = E_L \cos(\omega_L t), \tag{5-2}$$

respectively. Here, E_s is the amplitude of the imaged signal and ω_s is its angular frequency. Likewise, E_L is the peak amplitude of the local oscillator and ω_L is its angular frequency. For heterodyne detection, we offset our LO frequency ω_L from ω_s by our choice of intermediate frequency ω_{IF} , such that:

$$\omega_{IF} = \omega_s - \omega_L \tag{5-3}$$

and the corresponding current output of the photodiode is

$$I_{PD} = \frac{2\eta e}{hf}\sqrt{E_s E_L}\cos(\omega_{IF}t + \phi), \tag{5-4}$$

where $\frac{\eta e}{hf}$ describes the efficiency of the photodiode to convert optical energy to electrical current.

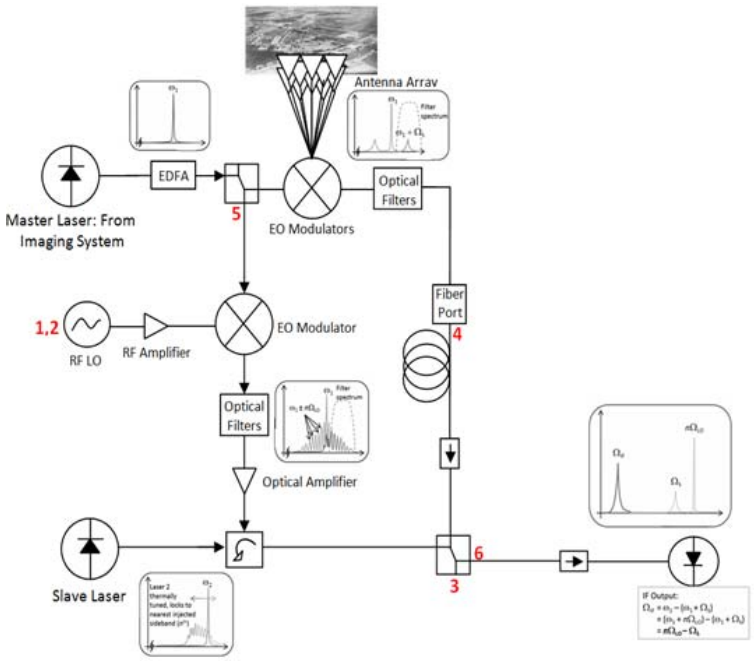

Figure 5-1: Schematic of optical LO used within receiver architecture

System Metric	Preliminary Test Result	Predicted Performance
Input Signal Range	34-38 GHz	26-40 GHz
Signal Bandwidth	2-4 GHz	Exceeding 10 GHz
IF	250 MHz – 5 GHz	1 – 15 GHz
Gain	-25 dB	> 10 dB
Noise Figure	35 dB	10 dB
SFDR	100 dB/Hz	125 dB/Hz

Table 5-1: Table of measured and predicted performance of system with upgrades

Through optimizations and upgrades to our receiver architecture as discussed in Chapter 7, predicted performance metrics show vast improvements compared to our current test results as depicted in Table 5-1 though LO heterodyne detection. Figure 5-2 displays an image of the front side of the rackmount chassis, matching the above schematic with the correct input and output RF and optical ports,. As seen, we are able to monitor the RF spectrum as well as the optical spectrum at the IF output.

Figure 5-2: Front panel display of RF and optical adapters for connectivity to imaging receiver

5.2.1 Parts Required for Optical Down-Conversion

The components required to design the LO for operation with the imaging receiver are listed and detailed in the below paragraphs. Figure 5-3 overviews the components built together inside the LO sub-system. A 2U (16.60" x 18" x 3.50") rackmount chassis was used to minimize SWaP of the system, while still maintaining appropriate thermal release. The recovered signal is connected to an optical path length (OPL) matching fiber to match the path length of both arms; the injection-locking arm and the imaging system arm to suppress the phase noise and reduce the linewidth of the generated IF signal to ~1 Hz.

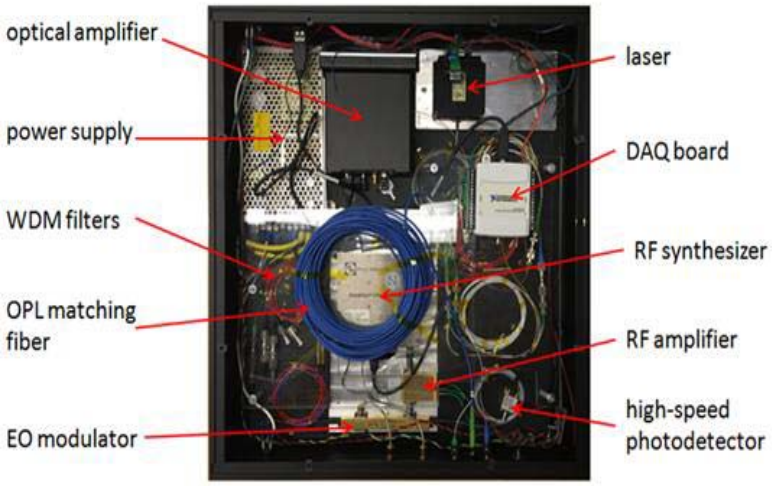

Figure 5-3: Top view of optical LO with labeled components

The first component is the RF synthesizer. This component was bought through Phase Matrix (FSL-0010) to act as our low frequency synthesizer. This is a lite model synthesizer with minimal functionality. The synthesizer is only capable of tuning frequency between 650 MHz to 10 GHz. For the purpose of setting the IF

output, the Phase Matrix offered superb phase noise, pure frequency stability, and low SWaP operation.

The second component is the RF amplifier. The RF amplifier used is a Picosecond Pulse Labs (5882-206) 16 dB gain amplifier. The low gain amplifier was chosen to operate in its non-linear regime while not adding excessive gain to all harmonics of the input RF tone. Current draw from this amplifier is significantly lower than the RF Lambda amplifier reducing the thermal dissipation in the system.

The third component is the optical modulator. The modulator used is a phase modulator from Thorlabs (LN66S-FC). This modulator was chosen instead of an amplitude modulator so we did not have to concern ourselves with biasing for carrier suppression. This is a 40 GHz bandwidth modulator, capable of high frequency modulation generation. The output of the modulator is sent through 100 GHz WDM optical filters to filter out the lower sidebands along with the carrier as they are unused. The non-filtered portion of the optical spectrum is then amplified through an optical amplifier to send the appropriate locking strength of the injected sideband.

Similar to the TOPS generator, a booster optical amplifier was chosen to amplify the pass-band sidebands. The BOA was purchased through Thorlabs (BOA1004P) along with the LD/TEC controller (CLD1015). After the filters, the sidebands are too weak to be injected-locked in the slave laser, so the BOA acts as the medium between these two optical pieces of equipment. By amplifying the sidebands enough, weak injection locking is possible. Higher optical current settings are required at high frequency offsets of the modulator, such as 35 GHz, where we used the 5^{th} harmonic of 7 GHz.

The most critical component to the optical LO is the slave laser. This laser was purchased through Gooch and Housego (EM651-192500-100-PM900-FC-NA). It is a 100 mW packaged module without an isolator. Rather than a 14-pin butterfly configuration, we chose a package module to compare laser capability. The laser is tuned according to its temperature voltage, V_{ta} setting, approximately equating to 100 GHz tunability. Unfortunately, the laser does not have a built in TEC, meaning there is no thermal stability. As a result, during emission, the wavelength can vary slightly over the entire process of running the LO causing instability in the injection-locking process. To control the laser, enable and frequency adjust is tuned by altering the voltage on a DAQ.

A LabVIEW program was created to control the main components of our system, specifically the BOA, RF synthesizer, and the laser controlling DAQ. Individual control of each component allows for precise up-to-date control of the LO to ensure continuous locking and stable laser emission to operation with the communication receiver for downconversion. As an added capability, automated tunability to any IF output is possible through the LabVIEW program.

5.3 Initial Results

An initial test was demonstrated to verify coherent detection and downconversion of a single TOPS signal. In this specific test case, the TOPS were set to emit RF at 35 GHz aimed at the imaging receiver from 2 meters away. To fully grasp the capability of our receiver architecture to receive and downconvert an incoming signal to an IF, the optical LO was tuned and locked to the 5^{th} harmonic of 6 GHz off of the master laser sourcing the antenna channels. Given the RF radiation was set at 35 GHz and the LO set at 30 GHz, an IF output of 5 GHz was expected on an

RF spectrum analyzer after mixing on a photodetector. Figure 5-4 displays a screen capture of the 5 GHz signal realizing the capability of photonic heterodyne downconversion using an injection-locked optical source. The slight frequency offset from 5 GHz is attributed to the TOPS synthesizer not reference locked to the LO synthesizer. Additional tests demonstrated the capability to tune the IF to lower frequencies for baseband detection on Oscilloscopes and other analysis equipment.

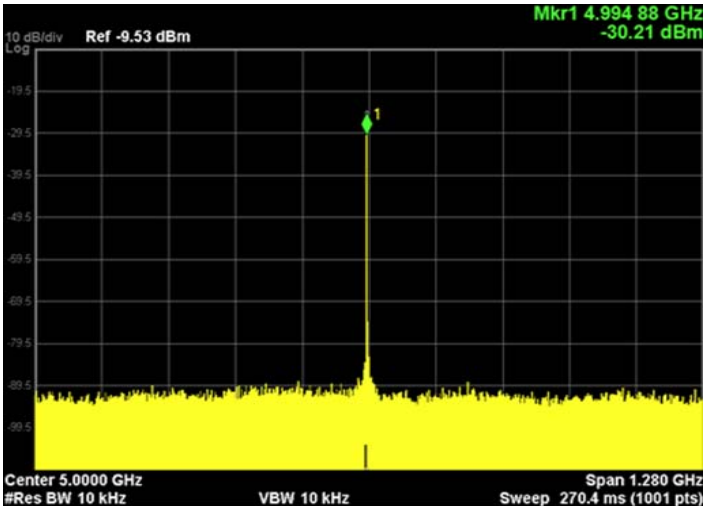

Figure 5-4: Downconverted RF from 35 GHz to 5 GHz using an optical LO

Chapter 6

WIRELESS COMMUNICATION IMAGING AND DETECTION

6.1 Introduction

RF signals produced through TOPS generation or electronic oscillation are not normally suitable for direct transmission of various information formats over specific frequency bandwidths. These signals are usually further modified to facilitate communication transmission. The conversion process to convert a given frequency channel to contain added information is known as modulation [38]. Through all different modulation parameters, complex formats are possible to be transmitted at ultra-high frequencies with increasingly large bandwidths. In order to generate a modulated signal, the sinusoidal high frequency carrier is typically varied by one of its parameters, such as: amplitude, frequency, or phase. Hence, these parameters derive modulation formats such as amplitude modulation (AM), frequency modulation (FM) and phase modulation (PM).

However, engineering constraints are placed at the receiver end to process such modulation schemes. A demodulation method must be designed to reverse process the modulated RF signal to reconstruct the original communication information. Additionally, concerns rise in environments where analog and digital transmissions are evident. Analog communications are best described as continuous data signals through time and value, but experience degradation in noisy environments. Alternatively, digital communications are binary represented signals more susceptible to noise, where noise can affect the bit error rate of the system, but naturally incur greater SNR compared to analog signals as digital communication systems have feedback

prevention loops to eliminate corrupted bits. Digital systems require additional demodulation processing equipment to decode simultaneous amplitude and phase information, whereas, AM and FM systems are capable of utilizing a standard clock radio as the receiver and demodulator.

In the below subsections, we detail the progress and efforts towards characterizing our imaging receiver for detection and recovery of both analog and digital communication signals. In the cases discussed, all tests were taken between 1.6 to 1.7 meters from the receiver with a second source separated from the signal of interest by 2-5 inches, out of the realm of the angular resolution. In certain cases, specifically digital and FM testing, the second source was set at the same frequency as the original TOPS to prove CCI suppression. Further performance tests are currently ongoing to enhance the overall capability and bandwidth capacity of the imaging receiver.

6.2 AM Modulation Recovery

Initial demonstrations involved AM recovery through our imaging system. To refresh, the modulated RF is received by our imaging system and beam steered to be center focused on the detector port. For amplitude modulation, the optical sideband fluctuates in peak amplitude analogous to the change in amplitude strength of the music or audio tone. The recovered sideband is routed to a low speed photodiode for optical-to-electrical conversion. Due to coupling loss in the detector port, the converted signal was sent to a transimpedance amplifier (TIA) for additional current gain. The output of the TIA was then relayed to a generic speaker with auxiliary input. The AM radio demonstration setup is illustrated in Figure 6-1.

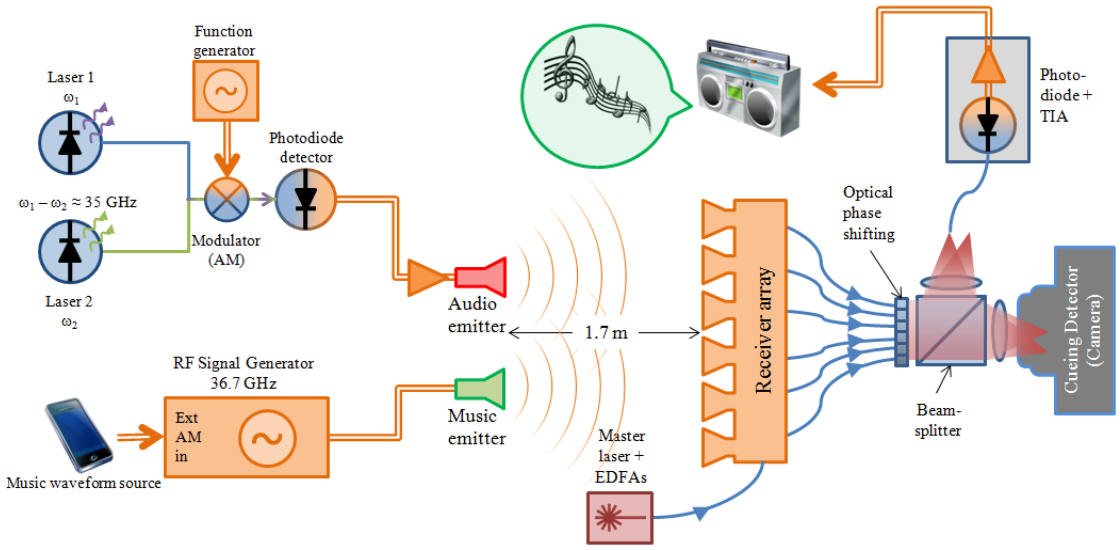

Figure 6-1: Photonic demonstration setup for spatially isolated AM recovery and detection using TOPS as an audio transmitter

The setup for the two transmitted sources can be seen in Figure 6-2 (left). First, the output of the TOPS was sent to an EO space 40 GHz amplitude modulator. The modulator was driven by an AM audio tone generated by an Agilent 33220A Arbitrary Waveform Generator. The music transmitter carrier was produced using a tunable Agilent microwave analog signal generator, N5183A. Taking a common music player, we were able to connect the output to the external AM port on the microwave source. The music transmitter was relayed to a horn antenna via RF cable, whereas the output of the EO modulator was sent to a high-speed 40 GHz U^2T photodiode for electrical conversion. Since the power handling of the photodiode was poor, we placed a Picosecond amplifier before the horn antenna for extra gain. The two antennas and the spacing between them are shown in Figure 6-2 (right). Adjacent channel interference was considered during preliminary testing for proof of concept of spatial isolation of

wireless communication signals by setting the frequency of the TOPS and microwave generator at 35 GHz and 36.7 GHz, respectively.

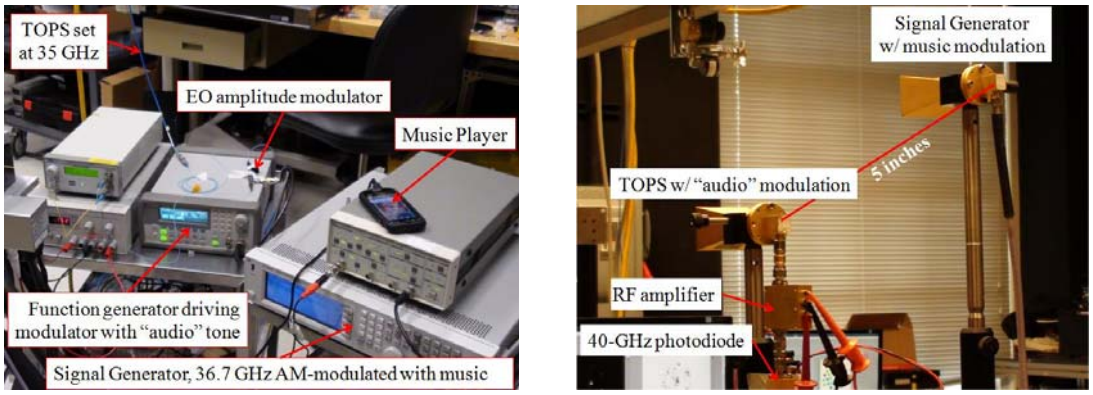

Figure 6-2: Equipment setup to generate two RF tones with AM transmitted data (left) and antenna setup for both sources with labeled spatial separation (right)

AM recovery experiment setup is illustrated in Figure 6-3 below. It is clear the distance between the transmitters and receiver is 1.7 meters away. The zoomed in image at the right of Figure 6-3 is the cueing detector image of both sources with the music transmitter centered on the image and the detector port. The varying detected energy was routed to a speaker for audible analysis. Sidelobe energy is evident on the cueing detector image and affected the spatial isolation of the system as the audio tones sidelobes fell in the resolution of the imaging receiver causing "ghost" images that both sources overlapped each other at the music transmitter's location.

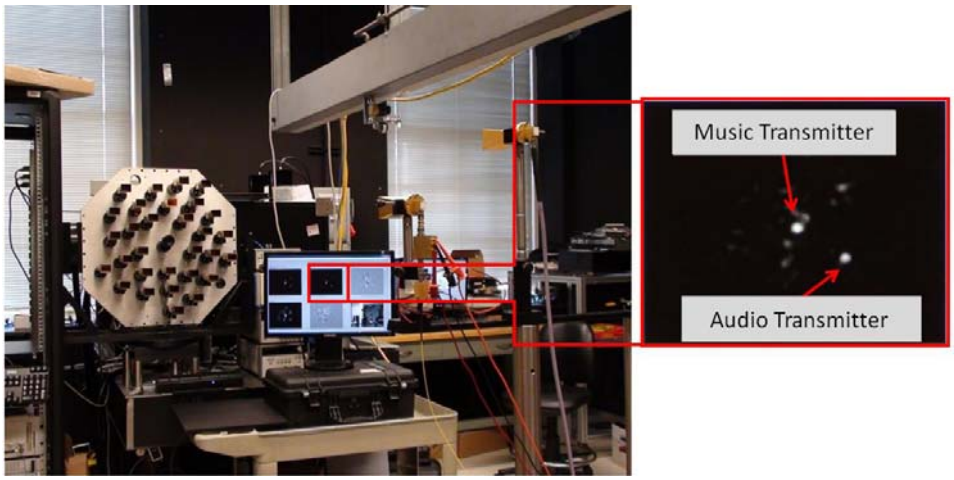

Figure 6-3: Two tone receiver setup with the imaging receiver beam steered toward the music transmitter (left) and the cueing detector image of the two sources with the music transmitter centered on the image (right)

6.3 FM Modulation Recovery using the Optical LO

Extending the capability of the system, we transitioned to frequency modulation, FM. Shifting our focus to FM offered numerous advantages. First, it showed that our communication receiver was be capable of analyzing a more complex modulation format, while demonstrating the ability to achieve continuous downconversion with a coherent optical LO. In terms of advantages, FM offers significantly greater resilience to noise as noise is primarily amplitude based and is removed since FM considers only the modulation variation of frequency. Also, FM does not suffer from audio amplitude fluctuations as the signal strength changes, which improves the sensitivity of the demodulation. However, instead of direct detection on a photodetector, FM requires more complicated demodulation schemes by implementing downconversion techniques to frequencies within the MHz band, especially for audible analysis. To fully understand the purity of the FM signal, Figure 6-4 displays the schematic for LO integration to achieve baseband IF generation.

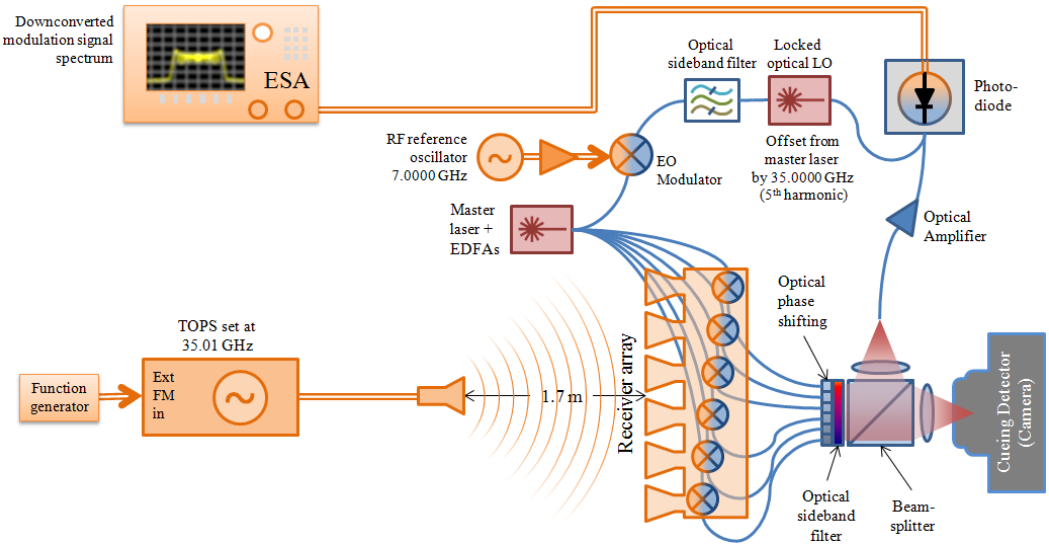

Figure 6-4: Photonic downconversion demonstration setup with an FM audio tone transmitting at 35.01 GHz RF carrier and mixed on a photodiode with the optical LO to an IF of 10 MHz

Here, a TOPS generator was set at 35.01 GHz with external Frequency modulation from a function generator. Given FM contains user specified IBW, we decided to analyze a single source to avoid any noise of SNR contributors from CCI and ACI sources. The recovered energy was mixed with the LO set at 35 GHz. After heterodyne detection on the photodetector, an IF of 10 MHz was generated. The generated downconverted signal was then relayed to an Agilent N9030A spectrum analyzer for processing. Figure 6-5 confirms the IF signal at 10 MHz with the music transmitter's instantaneous bandwidth and modulated tone. The RF spectrum analyzer was set to an average trace type as well as detector type to remove the excess RF noise to determine the exact recovered signal. From the image, the variation in ripples is determined by the FM deviation while the signal strength is determined by the FM amplitude into our TOPS and the signal strength of the downconverted IF tone.

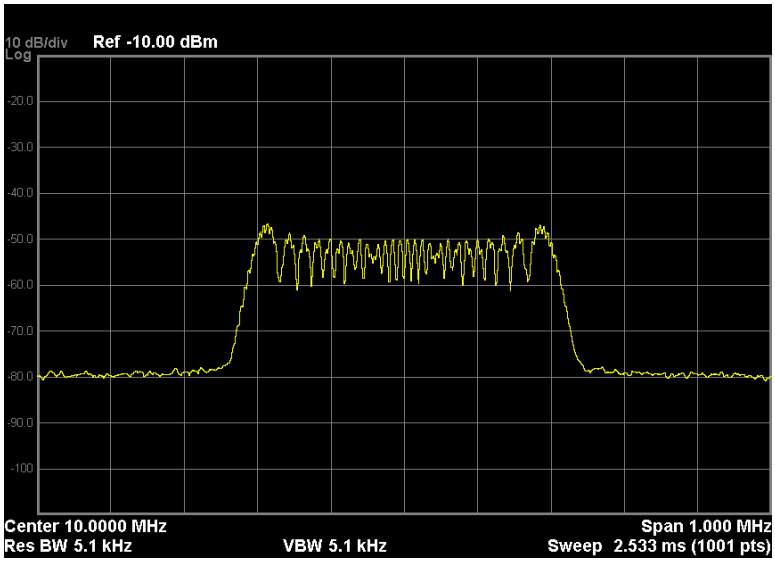

Figure 6-5: Recovered signal at a 10 MHz IF on an RF spectrum analyzer illustrating the signals IBW

For audible analysis, FCC regulated frequency analysis lies within the allocated radio bands. In order to achieve IF generation between 88 to 108 MHz, we tuned the transmitter to be offset by the LO to within this frequency band. By replacing the RF cable between the photodiode and the RF spectrum analyzer with a FM free space antenna, we were able to use a clock radio to set the demodulator to hear our transmitted tone. Tests were demonstrated to prove obscurant avoidance wirelessly. We were able to conclude that little to no attenuation was apparent in the audible amplitude when plastic sheeting was placed in the RF free space path of the transmitter. Secondary testing included simultaneous transmission of an "audio" CCI source. Demonstrations concluded sufficient spatial isolation of the FM music transmitter from 2.5" away. Phase steering to the CCI tone suppressed the original

transmitter and confirmed demodulation and audible hearing of the CCI source instead.

6.4 Digital Modulation Recovery and Processing using Vector Signal Analysis (VAS) Software

Recently, we have demonstrated and characterized the versatility of our receiver system to recover complex modulated digital communication signals with appreciable data rates. To do so, the RF spectrum analyzer basic detection allowed analysis up to only 10 MHz bandwidth. Instead, we used a Keysight Infiniium Oscilloscope (DSOS204A), where information capacity up to and exceeding 2 Gb/s on 4 channels are possible. In terms of the demodulation process, we purchased Vector Signal Analysis (VSA) software from Keysight with hardware connectivity and digital demodulation secondary licenses. Two channels were used to demonstrate the comparison of a conventional receiver to our phased-array receiver. The first channel was an IF photo-mixed signal from the receiver and the second derived from the IF output of the RF spectrum analyzer for high-frequency direct RF detection in free space. A standard 20 dB gain horn antenna from Ducommun Technologies was mounted to our antenna array and routed to the RF spectrum analyzer via an RF cable.

Key metrics considered during our testing of CCI avoidance imaging included SNR of the demodulated communication signal, RF spectrum degradation, error vector magnitude (EVM) of the demodulated signal, and total data capacity throughput. To reiterate, in terms of receiver system SNR, it is determined by,

$$SNR = \frac{P_t G_t \left(\frac{\lambda}{4\pi R} \right)^2 G_r}{KTB_w f}, \tag{6-1}$$

where P_t is transmitting power, G_t and G_r are transmit and receive antenna gain, and B_w is the bandwidth of the received signal. Incorporating the SNR into Shannon's channel capacity theorem [39], the total achievable data rate is

$$C_D = B_W \log_2(1+SNR)\,. \tag{6-2}$$

EVM and RF spectrum degradation was determined through the VSA software demodulation process. Preliminary wireless digital communication experiments followed the demonstration setup configured in Figure 6-6. To fully comprehend our receiver approach, the interference source from the below Figure was turned off, mitigating any interference concerns.

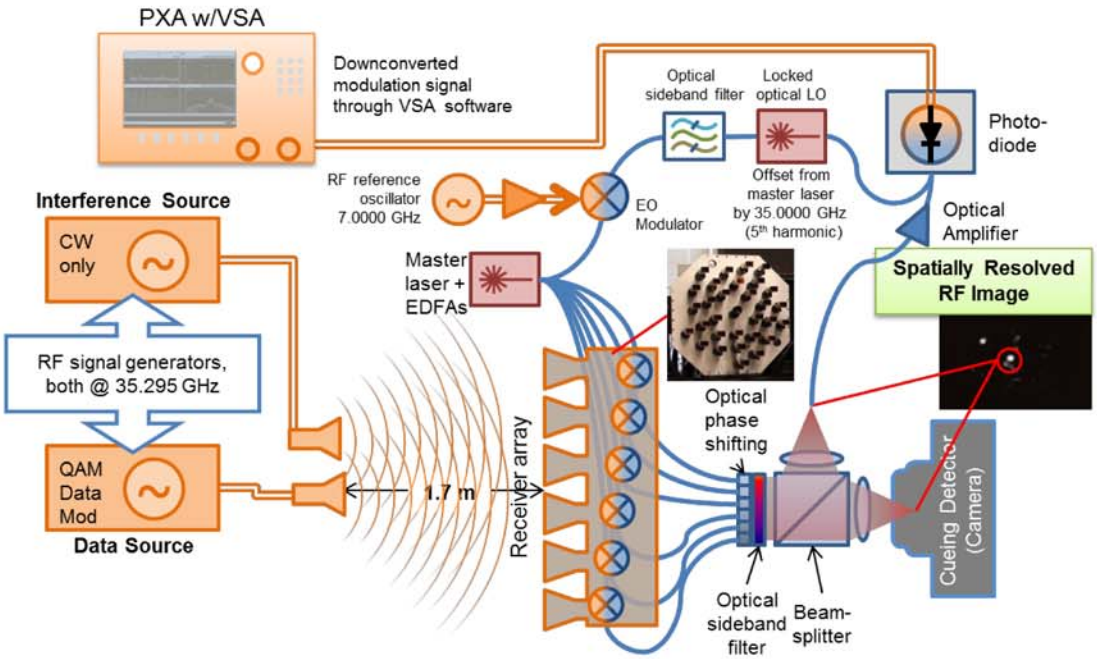

Figure 6-6: Photonic downconversion demonstration of communications signal recovery in the presence of co-channel interference

6.4.1 QAM Analysis

Fundamental testing began with a basic 4 Quadrature Amplitude Modulation (QAM) signal at a symbol rate of 1 Msps. Given 4 QAM equates to 2-bit operation, a total data capacity of 2 Mb/s transmission was successfully demodulated through our communication receiver. The transmitted signal was received through our receiver, and downconverted with our optical LO to an IF of 295 MHz for sufficient bandwidth operation at baseband through our Oscilloscope. Through VSA software demodulation, Figure 6-7 (left) demonstrates the 4 QAM I-Q constellation of the recovered signal and the corresponding RF spectrum showing the 1 MHz associated bandwidth of the signal (right). As proof of concept detection, we determined our receiver is capable of identifying a digitally modulated emitter in the scene and able to recover and process the contained information.

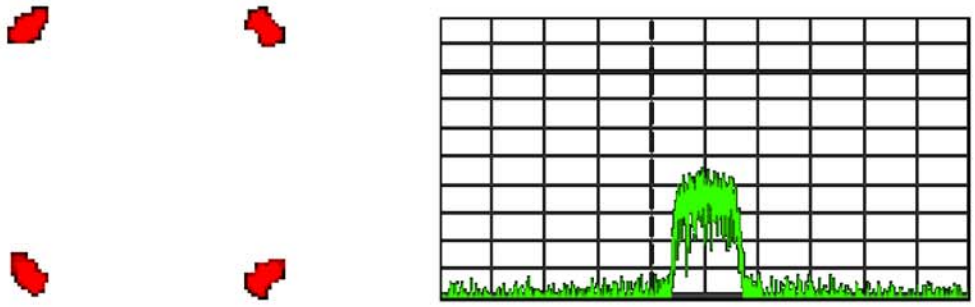

Figure 6-7: Preliminary 4 QAM demodulated signal with 1 Msps symbol rate (left) and corresponding RF spectrum illustrating the signal bandwidth (right)

Subsequent analysis involved examining noise contributors that prove detrimental to detrimental to the I-Q constellation. First, SNR of 20-25 dB is sufficient wireless demodulation to observe the correct constellation, however, causes

error in the ability of each point to locate the center position of its symbol accurately. Poor SNR is attributed to coupling loss in the optical sideband detector port and excess optical noise from the EDFAs and BOA of the optical LO. Also, due to imperfection in path matching between the optical LO arm and the imaging receiver, phase error greatly impacts the constellation by elongating each symbol, especially at the edges A. Moloney, "Channel Capacity," *Channel Capacity*. [Online]. Available: http://www.electronics.dit.ie/staff/amoloney/dt008_2/dig-comms-ii-lecture-11-12.pdf.

[40]. Figure 6-8 (left) shows a typical free space demodulated 16 QAM signal demonstrating a minimal noise contributing signal with high SNR compared to Figure 6-8 (right) that shows the phase error imbalance of the symbols as well as the poor SNR contribution to the constellation. By implementing a better path matching fiber optic cable and increasing the transmit power of the digitally modulated signal, we were able to combat these error effects for improve QAM receiver performance.

Figure 6-8: Illustration of path matched RF with no associated phase noise (left) and inherent phase noise contribution from communication receiver due to optical fiber path mismatch (right)

Digital modulation performance analysis included demonstrating the ability of the receiver to detect higher modulation rates and symbol rates, at the expense of poorer SNR. Overall, increased bandwidth is directly proportional to data capacity. By

optimizing the receiver and detector port to increase the SNR of the optical sideband before photodetection, we were able to increase the symbol rate to 50 Msps, or a 50x improvement in data capacity of the wireless link. By improving the bit rate from 4-bit, 16 QAM, to 5-bit, 32 QAM, or 6-bit, 64 QAM, we were able to improve our data rate capacity from 4 Mb/s to 300 Mb/s. Although some points experienced major error causing overlap of neighboring symbols, it is evident from Figure 6-9 that 32 QAM and 64 QAM data rates are possible according to their constellations. With further improvements to SNR, we expect accurate containment of points within their respective symbols.

Figure 6-9: Demodulated 32 QAM (left) and 64 QAM (right) recovered through the imaging receiver at 50 Msps symbol rate

6.4.2 CCI Isolation Results

More recently, we have demonstrated the ability of our communication receiver topology to spatially suppress co-channel interference as shown in Figure 6-10. It is evident from Figure 6-10 (left) that the second interference source is suppressed below detection strength compared to the communication signal of interest

due to its different angle-of-arrival at our antenna array compared to Figure 6-10 (right) where the carrier strength of the interference signal is co-dominate in the RF spectrum at the reception of the free space horn antenna. Spatial multiplexing capabilities experience minimal signal degradation compared to its conventional free space antenna counterpart.

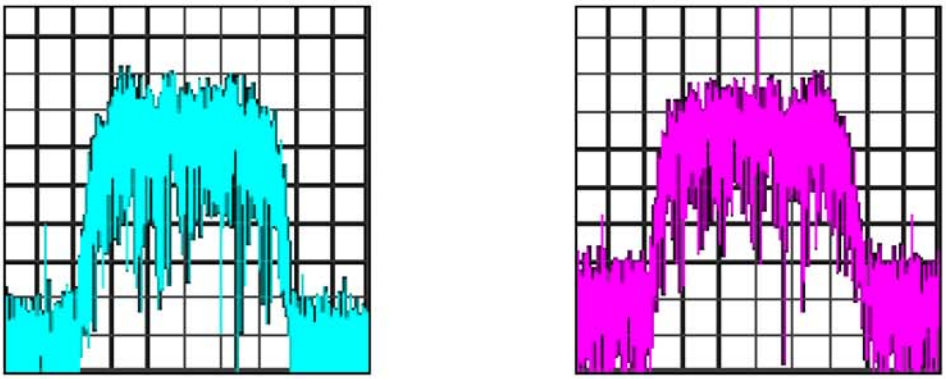

Figure 6-10: Downconverted IF spectrum with CCI suppression through communication receiver (left) and co-channel carrier spectrum interference through a conventional free space antenna (right)

Table 6-1 displays the effects of CCI on both error vector magnitude and signal-to-noise ratio. Clearly, SNR through the conventional receiver is severely damaged compared to 3 dB loss experienced in the imaging receiver. The 3 dB loss is attributed to poor diffraction efficiency of the receiver as plotted in Chapter 2. Similarly, the EVM percentage increases by 51.5% rms, whereas the imaging receiver experienced a minor 2 % rms hit when in the presence of CCI.

	Without CCI		With CCI	
	Conventional Receiver	Imaging Receiver	Conventional Receiver	Imaging Receiver
Error Vector Magnitude (EVM) (% rms)	7.2215	4.5687	58.813	6.5844
Signal-to-Noise (SNR) (dB)	22.827	26.804	4.611	23.63

Table 6-1: EVM and SNR Data at 16 QAM with and without CCI

Lastly, the introduction of CCI completely destroys the I-Q constellation of the free space detector. By using the Keysight Oscilloscope, we were able to test two channels simultaneously through VSA digital demodulation. Testing at 4 QAM and 16 QAM modulation rates with a bandwidth of 50 MHz, results were recorded to determine the validity of our SDM receiver approach. As shown in Figure 6-11, when the second interference source is turned off, the I-Q constellation of both the conventional receiver and the imaging receiver mirror each other closely, with slight differentiation in phase error and SNR mismatch to cause the disparity. Without CCI, 100 Mb/s and 200 Mb/s is achievable through both detection schemes. However, in the presence of a second interference source, as stated earlier, through spatial isolation of the receiver we are able to recover the transmitted TOPS data at little to no I-Q alteration, whereas the experienced damage to the constellation in the free space horn antenna is immense making digital signal recovery unfeasible.

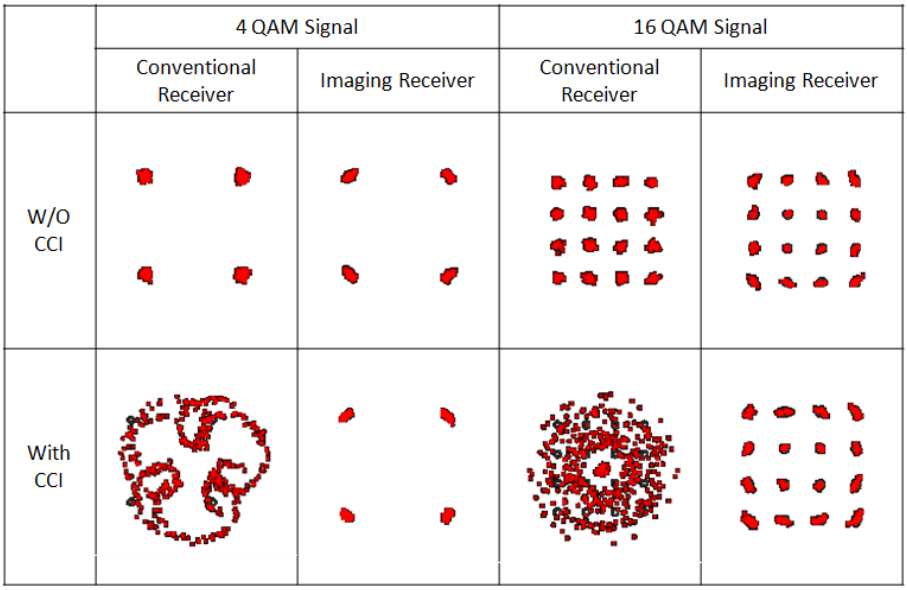

Figure 6-11: 4 QAM and 16 QAM at 50 Msps symbol rate with and without the presence of a second CCI transmitter

Chapter 7

CONCLUSIONS

Microwave Photonics is a rapidly maturing field that combines both the RF and optical regimes. To this extent, link communications research is transitioning to Microwave Photonics rather than solely electronics. Developments of communication receivers capable of unlimited bandwidth, spatial multiplexing, and robust configurations require highly precise and specialized equipment only possible through optics. As a result, designing such receivers with high data capacity throughputs are able to locate and detect each transmitted communication signal with sufficient SNR is extremely demanding and difficult. To this end, we have presented a novel approach towards developing and characterizing an optically addressed millimeter-wave receiver for wireless communications. The design of TOPS has allowed us to optically generate any RF frequency with encoded QAM data to act as a low cost, high fidelity transmitter. Through AoA detection enabled by beam-steering capabilities, we are able to spatially isolate each incoming TOPS signal to its own spot on the camera as well as decode the data stored on the up-converted carrier by photomixing with an optical LO for baseband signal analysis. We have demonstrated data rates up to 300 Mb/s, while current research efforts are taking place to optimize the imaging receiver so data rates up to and exceeding 10's Gb/s data capacity may be detected. In addition, improvements to the SWaP of the system can be made to package and construct more desirable systems for military and civilian use.

7.1 Receiver Improvements and Optimizations

Currently, poor signal-to-noise and prototype system level designs have been demonstrated for this approach. Fortunately, improvements and optimizations can be made to ultimately achieve unlimited bandwidth as well as small form factor, cost effective systems for use in 5G wireless networks.

Signal-to-noise is extremely crucial to detect and analyze each incoming signal. Worse SNR results in less probability of understanding the information contained. Components that are currently limiting our imaging systems ability to achieve high SNR are: laser performance, coupling of the recovered signal, and RF amplification and bandwidth. To start, a poor performing laser gives way to high optical noise resulting in high RF noise. In our current architecture, we use an Agilent 81682a 1550 nm tunable laser. Originally bought for tunability around the optical filters for stronger optical energy throughputs, it has now led to high noise contributions from the RIN of the laser, as well as the poor OSNR. Replacing the current laser with a much greater performing laser would achieve lower optical noise, reaching a shot noise limited system rather than a RIN limited system. While achieving lower noise, a high-powered laser would eliminate the need for EDFAs. Removing EDFAs from our system would remove the added spontaneous noise apparent in the amplifier as well as the additional noise figure attributed to each EDFA. Thus, converting from optical to electrical, our RF noise would significantly drop as a result of lower optical noise increasing the total SNR of the system. Table 7-1 below shows the improvements of the Orbits Lightwave laser characteristics of reduced optical SNR with extremely low RIN values compared to our current Agilent laser.

Model	Agilent 81682a	Orbits Lightwave Ethernal
Wavelength and Range	C-Band Tunable λ	1557.62 nm +/- .02 nm (Fixed λ)
Output Optical Power	~5 mW	> 1.8 W
Linewidth	100 kHz	< 400 Hz
RIN	-145 dB/Hz	-165 dBc/Hz
Side Mode Suppression Ratio	>40 dBc	> 75 dBc
Signal to Noise Ratio	> 45 dBc	> 70 dBc

Table 7-1: Comparison of current Agilent laser characteristics to potential noise improvement with an Orbits Lightwave Ethernal laser

Remaining in optics to improve SNR, a better coupling port is necessary to reduce or completely eliminate the loss associated with the mode profile mismatch. As stated in an earlier section, a 20 dB loss is calculated from free space to the output of the coupled fiber requiring an extra EDFA to boost the signal back to its expected value. This 20 dB loss significantly lowers the signal strength, while the EDFA adds unnecessary noise to the overall system performance. In addition, we have only implemented a single detector port. This means, as stated earlier, only one TOPS signal can be detected and analyzed without phase-steering to the next signal location. A single photodetector vastly reduces the capability of our receiver to simultaneously image and demodulate all sources in the scene. Here, we have proposed the replacement of the single photodetector recovery port with a FPA receiver board comprised of photodetectors as an improvement. Essentially, specific pixels in the

scene will correspond to a photodetector on the FPA board. The array of detectors will allow the receiver to detect, down-convert, and analyze all incoming communication and radio signals instantaneously. Introducing an FPA board adds the ability to turn off specific sections of the scene to resolve solely the signals of interest, greatly improving the dynamic range and overall SFDR of the receiver. In comparison, conventional receiver architectures are unable to map sources to specific spatial locations prohibiting data channelization.

RF amplifiers have long been characterized and fabricated. However, performance metrics typically change according to specific needs. For passive imagery with our millimeter wave imaging system, it was necessary to obtain narrow bandwidth LNAs to remove fringe washing. Commercially available LNAs with a narrow frequency bandwidth were originally purchased, with the following specifications: 30-35 dB gain, 7 dB noise figure, and 3-5 GHz bandwidth centered at 35 GHz. Through noise figure measurements, these amplifiers proved to have worse NF than specified. For data capacity and throughput, low gain, high NF proves detrimental to the total RF noise figure, ultimately worsening the overall SNR of the system. Improving the gain of the RF front-end amplifiers while maintaining very low noise figure will positively impact the analyzed SNR of the received signals, leading to greater data capacities. Since RF free space path loss is extremely large at ultra-high frequencies, a higher gain amplifier will increase the received RF strength before the optical modulator, resulting in greater optical sideband energy. Combined with significantly lower noise figure - on the order of 4-6 dB - the input RF noise to the system can be drastically decreased, improving the output RF noise after photomixing. Recently, we purchased and executed performance metric testing of a potential

amplifier replacement. Figure 7-1 details the gain and noise figure improvements compared to our current KMIC amplifier. It is evident that the RF Lambda LNA offers significantly higher gain through all Ka band with noticeably lower noise figure. In total, the expected SNR of the recovered communication signal should boast a 15-20 dB improvement over the current results.

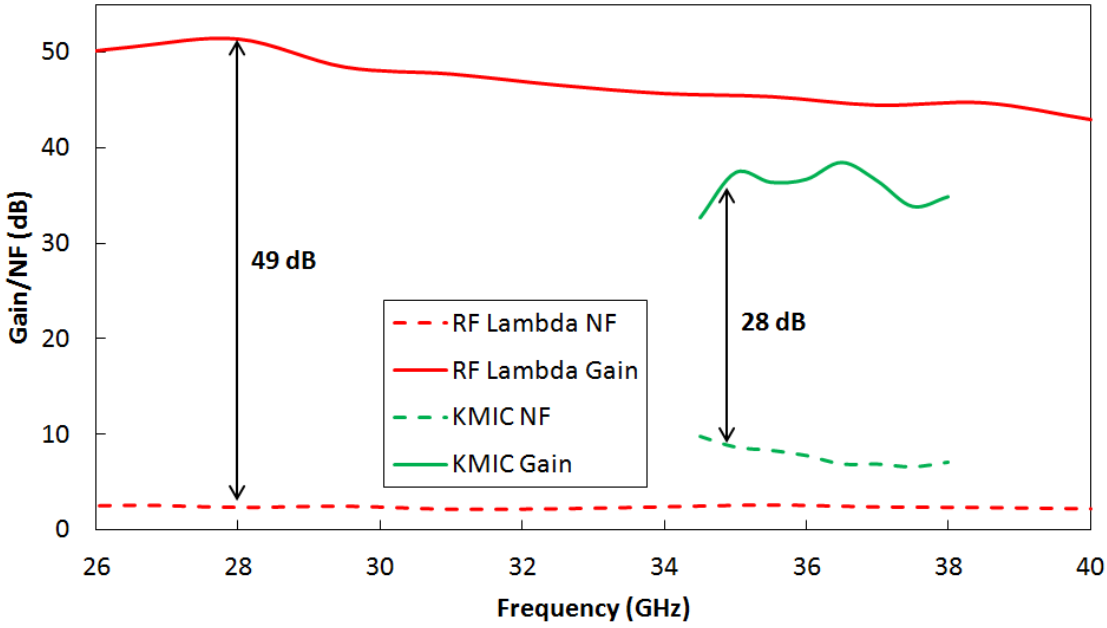

Figure 7-1: Amplifier comparison of current KMIC amplifier to improved RF Lambda amplifier for bandwidth coverage and better gain and NF characteristics

Ultimately, this substantial improvement to SNR should offer data rates up to 5-10 Gb/s as a standalone upgrade. Factoring in the laser upgrade and the reduction to coupling loss of the received optical energy, data capacities exceeding 100's of Gb/s are expected.

As technology advances, so does the demand for small form factor, low cost products. To this extent, research efforts have been made to reduce the CSWaP of our prototype receiver. Investigations into the weight and size reduction of the RF front-end modules are underway. Our current architecture utilizes bulky horn antennas as well as separately packaged amplifiers and modulators. Figure 7-2 below illustrates our current RF front-end module used within our communication receiver. Measured results concluded that our current module is 14" in length and has a 3" diameter with protrusions that set the minimum pitch of the array to about 4".

Figure 7-2: RF Front-End Module in current communication receiver

An alternate solution is to use multi-layer Liquid Crystal Polymer (LCP) substrates to include the listed RF and optical components contained in the current module. LCP has promising performance metrics in the millimeter wave regime while maintaining an ultra-small profile at extremely low cost. Figure 7-3 shows the paper-like LCP material and interconnected conductive layers that are possible to design within the structure [41]. Efforts have been made to design RF to optical front-ends in LCP at 94 GHz [42].

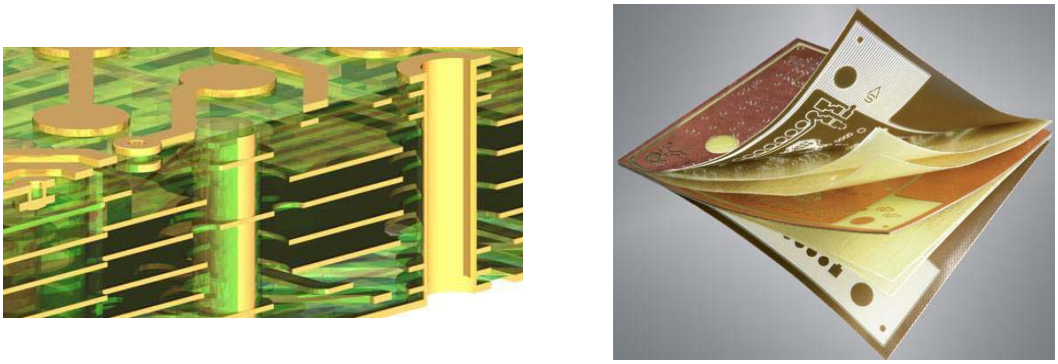

Figure 7-3: Conductive layers all interconnected to each other through coupling structures (left) [43] and the LCP material (right) [44]

SWaP improvements can be seen in Figure 7-4 below. Figure 7-4 (top) shows all of the RF components capable of being designed within the LCP multilayer structure. Clearly, the decrease in length from 14" to 4.9" is a major improvement to the size of the overall antenna array of the receiver. Weight has been documented to be reduced by more than 10x that of the current front-end. The reduced weight is attributed to removing the huge amplifier waveguide housing and large horn antennas. Similarly, power consumption was reduced significantly. Figure 7-4 (bottom) depicts the RF to optical coupling within a packaged device. Here, custom designed LNAs are wire-bonded onto the LCP substrate while the passive components are soldered directly to the substrate. The output of the microstrip to coplanar waveguide (CPW) is wire-bonded to a PSI fabricated modulator as described in Chapter 2 for ultra-high E/O conversion.

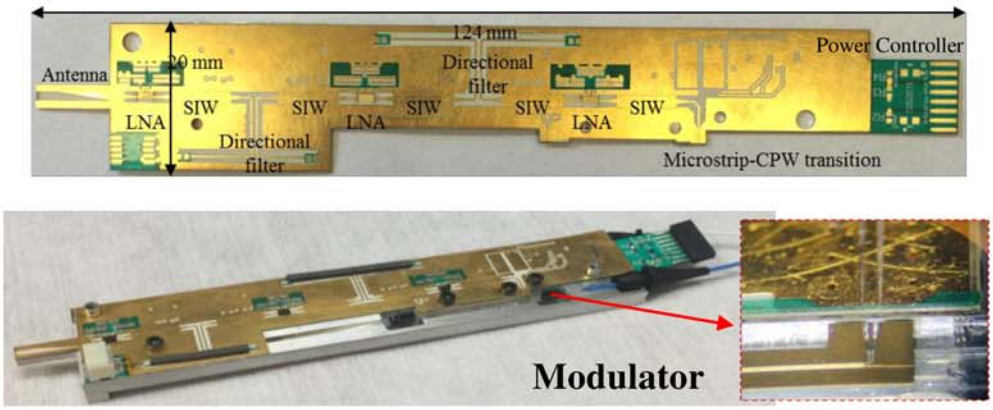

Figure 7-4: Detailed LCP module (top) and a packaged RF front-end module with integrated modulator (bottom)

By condensing the RF front-end into a smaller distributed aperture and reducing the free space optics to only the necessary components and lenses to generate our imagery while continually phase locking, our communication receiver has the potential to operate at an unlimited bandwidth with high SNR in a pizza box sized form factor, acceptable for 5G wireless networks.

7.2 Final Remarks

This thesis has covered a wide range of complex Microwave Photonic systems and components. Research efforts to detect and analyze wireless communication links have been achieved through the design of a TOPS source, optical LO, and an optically addressed receiver. Proper use and maintenance are important to keeping the systems well calibrated. As the communications environment begins to run out of usable bandwidth and signal isolation, a need for a new receiver paradigm is required. Current results as well as planned improvements confirm this type of imaging receiver is capable of being implemented as the next generation 5G wireless network receiver.

REFERENCES

[1] "Photophone," *Wikipedia, the free encyclopedia*.

[2] Michael Tsai, "Link Budget," 22-Sep-2011.

[3] F. Khan and Z. Pi, "mmWave mobile broadband (MMB): Unleashing the 3-300GHz spectrum," in *2011 34th IEEE Sarnoff Symposium*, 2011, pp. 1–6.

[4] C. Langton, "Link Budget," *Link Budget*, 2002. [Online]. Available: http://complextoreal.com/wp-content/uploads/2013/01/linkbud.pdf.

[5] J. Zyren and A. Petrick, "Tutorial on Basic Link Budget," *Tutorial on Basic Link Budget*, 1998. [Online]. Available: http://www.sss-mag.com/pdf/an9804.pdf.

[6] R. K. Tyson, "Bit-error rate for free-space adaptive optics laser communications," *Journal of the Optical Society of America A*, vol. 19, no. 4, p. 753, Apr. 2002.

[7] "Radar Basics - Phased Array Antenna." [Online]. Available: http://www.radartutorial.eu/06.antennas/Phased%20Array%20Antenna.en.html

[8] E. Fishler, A. Haimovich, R. Blum, R. Cimini, D. Chizhik, and R. Valenzuela, "Performance of MIMO radar systems: advantages of angular diversity," in *Conference Record of the Thirty-Eighth Asilomar Conference on Signals, Systems and Computers, 2004*, 2004, vol. 1, pp. 305–309 Vol.1.

[9] J. Brady, N. Behdad, and A. M. Sayeed, "Beamspace MIMO for Millimeter-Wave Communications: System Architecture, Modeling, Analysis, and Measurements," *IEEE Transactions on Antennas and Propagation*, vol. 61, no. 7, pp. 3814–3827, Jul. 2013.

[10] W. Fu, Z. Tao, J. Zhang, and D. P. Agrawal, "Clustering Based Fractional Frequency Reuse and Fair Resource Allocation in Multi-Cell Networks," in *2010 IEEE International Conference on Communications (ICC)*, 2010, pp. 1–5.

[11] D. Lee, H. Seo, B. Clerckx, E. Hardouin, D. Mazzarese, S. Nagata, and K. Sayana, "Coordinated multipoint transmission and reception in LTE-advanced: deployment scenarios and operational challenges," *IEEE Communications Magazine*, vol. 50, no. 2, pp. 148–155, Feb. 2012.

[12] W. C. Y. Lee, "Elements of cellular mobile radio systems," *IEEE Transactions on Vehicular Technology*, vol. 35, no. 2, pp. 48–56, May 1986.

[13] I. Koffman and V. Roman, "Broadband wireless access solutions based on OFDM access in IEEE 802.16," *IEEE Communications Magazine*, vol. 40, no. 4, pp. 96–103, Apr. 2002.

[14] S. Bellofiore, C. A. Balanis, J. Foutz, and A. S. Spanias, "Smart-antenna systems for mobile communication networks. Part 1. Overview and antenna design," *IEEE Antennas and Propagation Magazine*, vol. 44, no. 3, pp. 145–154, Jun. 2002.

[15] "KTH | Communication systems of the future." [Online]. Available: https://www.access.kth.se/en/newsandevents/2.11592/communication-systems-of-the-future-1.56063.

[16] T. E. Dillon, C. A. Schuetz, R. D. Martin, S. Shi, D. Mackrides, and D. W. Prather, "Passive Millimeter Wave Imaging Using a Distributed Aperture and Optical Upconversion," presented at the Millimetre Wave and Terahertz Sensors and Technology III, 2010, vol. 7837, 78370H.

[17] D. Mackrides, C. A. Schuetz, R. D. Martin, T. E. Dillon, P. Yao, and D. W. Prather, "Progress Toward a Video-Rate, Passive Millimeter-Wave Imager for Brownout Mitigation," presented at the DSS, 2011.

[18] T. E. Dillon, C. A. Schuetz, R. D. Martin, E. L. Stein Jr, J. Samluk, D. Mackrides, M. Mirotznik, and D. W. Prather, "Optical Configuration of an Upconverted Millimeter Wave Distributed Aperture Imaging System," presented at the Millimetre Wave and Terahertz Sensors and Technology II, 2009.

[19] J. Macario, P. Yao, S. Shi, A. Zablocki, C. Harrity, R. D. Martin, C. A. Schuetz, and D. W. Prather, "Full spectrum millimeter-wave modulation," *Optics Express*, vol. 20, no. 21, p. 23623, Oct. 2012.

[20] B. M. Overmiller, C. A. Schuetz, G. Schneider, J. Murakowski, and D. W. Prather, "Ultrabroadband phased-array radio frequency (RF) receivers based on optical techniques," 2014, vol. 8985, p. 89850U–89850U–8.

[21] R. Martin, C. Schuetz, T. Dillon, D. Mackrides, P. Yao, K. Shreve, C. Harrity, A. Zablocki, B. Overmiller, P. Curt, J. Bonnett, A. Wright, J. Wilson, S. Shi, and D. Prather, "Optical up-conversion enables capture of millimeter-wave video with an IR camera," *SPIE Newsroom*, Aug. 2012.

[22] Hakanson, E. "Phase-noise test options for wireless broadband" - Electronic Products. 51, 46-47 (2008).

[23] Schneider, G. J., Murakowski, J. A., Schuetz, C. A., Shi, S. & Prather, D. W. Radiofrequency signal-generation system with over seven octaves of continuous tuning. *Nat Photon* **7,** 118–122 (2013).

[24] X. S. Yao and L. Maleki, "Optoelectronic oscillator for photonic systems," *IEEE Journal of Quantum Electronics*, vol. 32, no. 7, pp. 1141–1149, Jul. 1996.

[25] P. Shen, N. J. Gomes, P. A. Davies, P. G. Huggard, and B. N. Ellison, "Analysis and Demonstration of a Fast Tunable Fiber-Ring-Based Optical Frequency Comb Generator," *Journal of Lightwave Technology*, vol. 25, no. 11, pp. 3257–3264, Nov. 2007.

[26] D. W. Grund, S. Shi, G. J. Schneider, J. Murakowski, and D. W. Prather, "Improved configuration and reduction of phase noise in a narrow linewidth

ultrawideband optical RF source," *Optics Letters*, vol. 39, no. 16, p. 4667, Aug. 2014.
[27] D. W. Grund, G. J. Schneider, J. Murakowski, and D. W. Prather, "Packaging and design of a heterogeneous dual laser chip for a widely tunable spectrally pure optical RF source," *Optics Express*, vol. 22, no. 17, p. 19838, Aug. 2014.
[28] P. Bhansali and J. Roychowdhury, "Gen-Adler: The generalized Adler's equation for injection locking analysis in oscillators," in *Design Automation Conference, 2009. ASP-DAC 2009. Asia and South Pacific*, 2009, pp. 522–527.
[29] D. W. Grund, G. A. Ejzak, G. J. Schneider, J. Murakowski, and D. W. Prather, "A Widely Tunable Narrow Linewidth RF Source Integrated in a Heterogeneous Photonic Module," *J. Lightwave Technol., JLT*, vol. 32, no. 7, pp. 1363–1369, Apr. 2014.
[30] S. Bansal and P. Kaushik, "Effect kf RF Linewidth on BER Performance of 64-QAM RoF," *International Journal of Advanced Technology and Engineering Research*, vol. 2, no. 2, Mar. 2012.
[31] L. A. Johansson and A. J. Seeds, "Millimeter-wave modulated optical signal generation with high spectral purity and wide-locking bandwidth using a fiber-integrated optical injection phase-lock loop," *IEEE Photonics Technology Letters*, vol. 12, no. 6, pp. 690–692, Jun. 2000.
[32] T. S. Rappaport, R. W. H. Jr, R. C. Daniels, and J. N. Murdock, *Millimeter Wave Wireless Communications*. Pearson Education, 2014.
[33] A. H. M. R. Islam, M. Bakaul, A. Nirmalathas, and G. E. Town, "Millimeter-Wave Radio-Over-Fiber System Based on Heterodyned Unlocked Light Sources and Self-Homodyned RF Receiver," *IEEE Photonics Technology Letters*, vol. 23, no. 8, pp. 459–461, Apr. 2011.
[34] S. Catreux, P. F. Driessen, and L. J. Greenstein, "Simulation results for an interference-limited multiple-input multiple-output cellular system," *IEEE Communications Letters*, vol. 4, no. 11, pp. 334–336, Nov. 2000.
[35] "Wiley: Fundamentals of Microwave Photonics - V. J. Urick, Keith J. Williams, Jason D. McKinney."
[36] J. M. Senior and M. Y. Jamro, *Optical Fiber Communications: Principles and Practice*. Financial Times/Prentice Hall, 2009.
[37] D. W. Smith, "Coherent fiberoptic communications," *Laser Focus*, pp. 92-106, November 1985
[38] B. P. Lathi, *Modern Digital and Analog Communication Systems*. Oxford University Press, 1998.
[39] A. Moloney, "Channel Capacity," *Channel Capacity*. [Online]. Available: http://www.electronics.dit.ie/staff/amoloney/dt008_2/dig-comms-ii-lecture-11-12.pdf.
[40] Z. Chen and F. F. Dai, "Effects of LO Phase and Amplitude Imbalances and Phase Noise on -QAM Transceiver Performance," *IEEE Transactions on Industrial Electronics*, vol. 57, no. 5, pp. 1505–1517, May 2010.

[41] Y. Zhang, S. Shi, R. D. Martin, and D. W. Prather, “Ultrawide band CBCPW to stripline vertical transition in multilayer LCP substrates,” *Microw. Opt. Technol. Lett.*, vol. 57, no. 6, pp. 1481–1484, Jun. 2015.

[42] Y. Zhang, S. Shi, R. Martin, P. Yao, K. Shreve, and D. W. Prather, “Multilayer liquid crystal polymer based RF frontend module for millimeter wave imaging,” in *2014 IEEE Antennas and Propagation Society International Symposium (APSURSI)*, 2014, pp. 1700–1701.

[43] “LCP Multilayer Circuit.” [Online]. Available: http://www.jycircuitboard.com/static/upload/images/pcb-multilayer-fabrication.jpg.

[44] Stefan Morl, “Thermoplastic circuit board,” *Functional Polymers*. [Online]. Available: http://polymer-engineering.de/en/research/fields/functional-polymers/thermoplastic-circuit-board.html.

Appendix

PUBLICATIONS LIST

[1] **B. M. Overmiller**, C. A. Schuetz, G. Schneider, J. Murakowski, and D. W. Prather, "Ultrabroadband phased-array radio frequency (RF) receivers based on optical techniques," 2014, vol. 8985, p. 89850U–89850U–8.

[2] R. Martin, C. Schuetz, T. Dillon, D. Mackrides, P. Yao, K. Shreve, C. Harrity, A. Zablocki, **B. Overmiller**, P. Curt, J. Bonnett, A. Wright, J. Wilson, S. Shi, and D. Prather, "Optical up-conversion enables capture of millimeter-wave video with an IR camera," *SPIE Newsroom*, Aug. 2012.

[3] M. R. Konkol, S. T. Kozacik, D. L. K. Eng, **B. Overmiller**, M. J. Zablocki, B. C. Olbricht, J. Murakowski, S. Shi, A. Sharkawy, and D. W. Prather, "Dual slot modulator for millimeter wave photonics," 2014, p. 898317.